LA-UR-18-29305 (Accepted Manuscript)

Coupled nonlinear elasticity, plastic slip, twinning, and phase transformation in single crystal titanium for plate impact loading

Feng, Biao
Bronkhorst, Curt Allan
Addessio, Francis L.
Morrow, Benjamin Mark
Li, W. H.
Lookman, Turab
Cerreta, Ellen Kathleen

To be published in: Journal of the Mechanics and Physics of Solids

DOI to publisher's version: 10.1016/j.jmps.2019.03.019

Permalink to record: http://permalink.lanl.gov/object/view?what=info:lanl-repo/lareport/LA-UR-18-29305

Coupled nonlinear elasticity, plastic slip, twinning, and phase transformation in single crystal titanium for plate impact loading

B. Feng , C.A. Bronkhorst , F.L. Addessio , B.M. Morrow , W.H. Li , T. Lookman , E.K. Cerreta

PII: S0022-5096(18)30921-9
DOI: https://doi.org/10.1016/j.jmps.2019.03.019
Reference: MPS 3594

To appear in: *Journal of the Mechanics and Physics of Solids*

Received date: 23 October 2018
Revised date: 17 February 2019
Accepted date: 22 March 2019

Please cite this article as: B. Feng , C.A. Bronkhorst , F.L. Addessio , B.M. Morrow , W.H. Li , T. Lookman , E.K. Cerreta , Coupled nonlinear elasticity, plastic slip, twinning, and phase transformation in single crystal titanium for plate impact loading, *Journal of the Mechanics and Physics of Solids* (2019), doi: https://doi.org/10.1016/j.jmps.2019.03.019

Coupled nonlinear elasticity, plastic slip, twinning, and phase transformation in single crystal titanium for plate impact loading

B. Feng[1], C. A. Bronkhorst[*1,2], F. L. Addessio[1], B. M. Morrow[1],
W. H. Li[1], T. Lookman[1], E. K. Cerreta[1]

[1]*Los Alamos National Laboratory, Los Alamos, NM 87545, USA*

[2]*Department of Engineering Physics, University of Wisconsin, Madison, WI 53706, USA*

Abstract High purity single crystal titanium (Ti) under shockwave loading in plate impact experiment is modelled and simulated, with help of the finite element. A thermodynamically consistent system of equations is formulated in the frame of large deformation to consider material anisotropy, rate dependence, and multi-physics including nonlinear elasticity, dislocation based plastic slip, deformation twinning, and phase transformation. A novel kinematics is proposed to consider phase transformation in the α twin variants and also to consider the dislocation based slip in all of components of parent material, primary twins and the ω phase. The thermodynamically consistent driving forces for plastic slip, twinning, and phase transformation are developed based upon the second law of thermodynamics. For nonlinear elasticity, the stiffness matrix is dependent on the volume fractions of all components, and the volumetric part of Cauchy stress is obtained from the nonlinear equation of state. Dislocation based plastic slip in multi-variant and multiphase heterogeneous materials is developed and interactions of dislocations among all slip modes are taken into account. A mechanism for dislocation density evolution during twinning and phase transformation is proposed. The shock loading along the [0001] and $\left[10\bar{1}1\right]$ directions of single crystal high purity Ti is investigated computationally. Very good correspondence between simulation and experiment is obtained, which includes pole figures, volume fractions of components, free surface velocity, peak pressure, and phase transformation pressure. Multiple experimental phenomena are interpreted based upon the progression of dislocation slip, deformation twinning, and phase transformation. In compression with the $\left[10\bar{1}1\right]$ crystal, a higher volume fraction in the primary twins but a

* Corresponding author.
Emails: cbronkhorst@wisc.edu (C. A. Bronkhorst); fengbiao11@gmail.com (B. Feng).
LA-UR-18-29305

lower secondary twin volume fraction in the [0001] crystal in experiment was observed. The higher propensity for phase transformation occurs in the [0001] crystal is reproduced. In addition to material texture, distributions of temperature, stresses, and plastic strains dependent on the impact loading directions are revealed.

Keywords: dislocation based crystal plasticity, deformation twinning, phase transformation, large deformation, shock loading, high pressure

1. Introduction

Modeling mechanochemical responses of solid materials to high-deformation-rate and high-stress loadings is of great importance and beneficial to material applications in space and aeronautic, automotive, defense, and nuclear energy industries. The group IV transition metal titanium (Ti) and its alloys have widespread and successful applications in these industries, due to highly attractive properties. The pressure-induced hexagonal close packed (HCP) (α phase) to hexagonal (ω phase) transformation in pure Ti has significant technological implications in the aerospace industry because this phase transformation lowers ductility and toughness (Sikka *et al*., 1982; Trinkle *et al*., 2003). Due to excellent corrosion resistance, Ti is considered as a candidate as nuclear waste container material for long-term storage (Shoesmith *et al*., 2000). With the properties of low density, high strength-to-weight ratio, relatively high melting point etc., Ti is a very attractive material for applications in the automotive industry (Sachdev *et al*., 2012). In addition, Ti has been increasingly used to either increase armor effectiveness or reduce the weight of current combat vehicles in the defense industry (Montgomery, 1997). To study Ti mechanochemical responses under shock loading (Bezruchko *et al*., 2006; Cerreta *et al*., 2006a and 2006b; Greeff *et al*., 2004; Jones *et al*., 2017; Morrow *et al*., 2017a and 2017b), the plate impact experiment is commonly used. In these experiments, velocimetry is frequently employed to measure the velocity at the rear free surface of the sample. During compression, the stress corresponding to the onset of phase transformation is often determined by the observation of a sharp kink in the velocity-time plots during loading (Morrow *et al*., 2017a). Ti during shock loading contains very complex microstructure variation, which includes dislocation slip, mechanical twinning, and phase transformations. It is well-known that the material microstructure significantly affects the material performance. Unfortunately, the surface velocity

is the only in-situ experimental data currently available, and the evolutions of material microstructure and stress and strain tensors are not available experimentally. Electron Backscatter Diffraction (EBSD) is commonly used for texture measurements of a recovered specimen after unloading. Consequently, the understanding of material microstructure and stress-strain responses in Ti during the high-deformation-rate and high-stress loading by modelling and simulation is of great interest and it is one of the main goals of this paper. This is also accompanied with interpretation of the limited experimental results available.

Modeling in meso-mechanical or single-crystal length scale is commonly employed to investigate deformation and texture evolution, which takes into account the characteristics of the single crystal and polycrystal and builds a bridge between the evolution of microstructures (e.g. dislocation and phase propagations) and macroscale deformation, failure, and damage. Over the last three decades, modelling single crystal deformation behaviors has been very successful but there are still many challenges remaining. For HCP crystal metals such as Ti, zirconium (Zr), and magnesium (Mg) under high strain rate loading, the complexity of mesoscale modeling for representation of the deformation and microstructure evolution originates from the anisotropy, rate dependence, and the coupled multiple physical responses (elasticity, plastic slip, plastic twinning, phase transformations, etc.). To the best of our knowledge, thermodynamically consistent mesoscale modelling of coupled dislocation slip, deformation twinning, and phase transformation in HCP metals is still absent. It is also challenging to consider all these physical responses in one model. Especially since there are multiple twinning and slip directions and different orders of twinning. In addition, the microstructure after loading is very sophisticated with over ten components of the deformation twins and omega phase possible from a single parent grain (see pole figures in this paper). Another goal of this paper is to develop a thermodynamically consistent system of equations to consider elasticity, plastic slip, twinning, and phase transformation for HCP metals.

Mesoscale modeling with coupled plastic slip and deformation twinning in HCP metals has been attracting researchers' attention for the last two decades. Tomé *et al*. (2001) proposed polycrystal constitutive equations with consideration of plastic slip and twinning for pure Zr deforming under static loading at room and liquid nitrogen temperatures. Salem *et al*. (2003, 2005) investigated twin-induced strain hardening of high-purity α Ti at room temperature, which

were incorporated into constitutive laws to describe the evolution of both twin and slip resistance. Beyerlein and Tomé (2008) developed a single crystal constitutive law for multiple slip and twinning modes for pure Zr, in which the evolution of the dislocation population explicitly depends on temperature and strain rate. Beyerlein and Tomé (2010) and Beyerlein *et al*. (2010, 2011) further develped a basic probabilistic theory for the nucleation of deformation twins in HCP polycrystalline Zr and Mg, where the grain boundary defects under stress were proposed as a controlling mechanism. Abdolvand *et al*. (2011, 2013 and 2015) incorporated deformation twinning in HCP metals into the crystal plasticity finite element method, in which the interaction between twin and parent grains was considered and played an important role in stress evolution inside the twin and even in thickening of twins. Wang *et al*. (2013) developed a physics-based crystal plasticity model including deformation mechanisms of both twinning and de-twinning for HCP metals. Niezgoda *et al*. (2013, 2014) modeled the twin nucleation as a stochastic process in the visco-plastic self-consistent framework for HCP metals. Zhang *et al*. (2018) investigated the stochastic competition in twin nucleation, twin growth and pyramidal slip in HCP single crystals under uniaxial compression along the *c*-axis. Ardeljan *et al*. (2015) modeled the morphological and crystallographic reorientation associated with the formation and thickening of a twin lamella in the framework of the crystal plasticity finite element method. Morrow *et al*. (2016) investigated the coupled slip and twinning in high purity single crystal Ti loaded in split Hopkinson pressure bar (SHPB) by using experiment and a self-consistent homogenization model. Cheng et al. (Cheng *et al*., 2018; Cheng and Ghosh, 2015, 2017; Ghosh and Cheng, 2018) formulated an advanced theory for discrete twin evolution and incorporated it into a crystal plasticity finite element model for Mg and its alloys. Hama *et al*. (2017) presented a crystal plasticity finite element method model to investigate the deformation behavior of a commercially pure Ti sheet under different strain paths. Kannan *et al*. (2018) studied the mechanics of dynamic twinning in single crystal Mg in combination with experiment and modeling. Feng *et al*. (2018a) proposed a thermodynamically consistent theory coupling elasticity, plastic slip, and twinning to study the deformation mechanism of single crystal Ti under SHPB loading conditions. One of the goals of this paper is to advance the constitutive theory presented in Feng *et al*. (2018a) to consider a Ti specimen loaded by plate impact by also accounting for phase transformation. Given that shock loading conditions lead to potentially

significant temperature evolution which affects all aspects of material behavior, this is also an additional feature of this work.

Ti phases and phase transformations have attracted tremendous interest both scientifically and technologically. At ambient conditions, the most stable phase of Ti is the HCP crystal structure (α phase) in space group $P6_3/mmc$. At ambient pressure and temperatures above 1155 K, the phase transforms to the high temperature phase (β phase) with body-centered-cubic crystal structure. At room temperature and under high pressures, the α phase transforms into another hexagonal structure called ω phase in space group: P6/mmm and No.191 (Hao *et al*., 2010), in the pressure range of 2.0-13.5 GPa (Jayaraman *et al*., 1963; Sargent and Conrad, 1971; Vohra, 1978; Sikka *et al*., 1982; Singh *et al*., 1982; Xia *et al*., 1990; Razorenov *et al*., 1995; Akahama *et al*., 2001, 2002; Vohra and Spencer, (2001); Cerreta *et al*., 2006a and 2006b; Saxena *et al*., 2015; Morrow *et al*., 2017a). Such a large pressure range for the $\alpha \rightarrow \omega$ transformation is caused by differences in the levels of material defects, impurity content, strain rate, stress states, and plastic deformation (Feng *et al*., 2017c and 2018b; Zhang *et al*., 2018). Xia *et al*. (1990) found that by using X-ray diffraction experiments the ω phase remains stable up to 87 GPa where transformation to the β phase occurs. Vohra and Spencer (2001) reported a novel unexpected transformation in Ti metal from the ω phase to an orthorhombic phase (distorted HCP, γ-phase) at a pressure of 116 ± 4 GPa. In this paper, the Ti sample is loaded at room temperature and the maximum pressure is below 15 GPa. Consequently, the $\alpha \rightarrow \omega$ transformation is only considered here, and the other high temperature and/or ultra-high-pressure phases (β and γ phases) do not exist under the conditions considered in this paper. Under moderately high pressures, the $\alpha \rightarrow \omega$ transformation of Ti and Zr are very similar and belong to the reconstructive class of phase transformation. The pathway of such phase transformation is very complex and is still a very active research area (e.g., Trinkle *et al*., 2003; Cerreta *et al*., 2005; Ghosh *et al*., 2014; Zong *et al*., 2014; Morrow *et al*. 2017a, b), and there are multiple suggested pathways for the $\alpha \rightarrow \omega$ transformation (e.g. Ghosh *et al*., 2014). By using molecular dynamics simulation, Zong *et al*. (2014) found that experimentally observed lattice rotation between α and ω phase is caused by deformation twinning in the α phase as a pre-cursor to phase transformation, while phase transformation itself does not contain salient lattice rotation. This is also consistent with experimental evidence from experimental pole figures as shown in

the results section, where the lattice rotation is small between the α component and its corresponding ω component. In our simulations, we follow this suggested pathway for transformation. There have been some mesoscale models representing the coupling between plasticity and phase transformations for HCP metals. Yeddu *et al*. (2016) formulated a three-dimensional elastoplastic phase-field model for the hydrostatic pressure-induced α to ω phase transformation and the reverse phase transformation in Zr. Zhang *et al*. (2018) developed a formalism of two-phase equilibrium and phase diagram for an elastic-plastic deformed system under non-hydrostatic stress conditions, which is applied to phase transition in Ti. Feng *et al*. (2017c, 2018b) studied the coupled plastic flow and strain-induced phase transition in Zr under high pressure and large shear in diamond anvil cells. In addition to coupled phase transformation and plasticity in Ti loaded by plate impact, a physically based model should also include the primary twinning and even secondary twinning, which are observed in Morrow *et al*. (2017a) and results reported in this paper.

There are three main goals for this paper. Firstly, it is to develop a thermodynamically consistent theory for coupled elasticity, dislocation slip, twinning, and phase transformation for HCP metals such as Zr and Ti. The driving forces for slip, twinning and phase transformation will be derived strictly from the second law of thermodynamics. Secondly, we will advance the constitutive theory presented by Feng *et al*. (2018a); (1) propose a nonlinear thermodynamics based elasticity rule for large elastic deformation. ;(2) the temperature evolution will be developed and implemented into the Helmholtz free energy, while it is considered as a constant in the work of Feng *et al*. (2018a).

Finally we use results of experiments conducted on single crystal Ti and loaded by high strain rate plate impact as a case study by using both the system of equations formulated in this paper and the finite element method (FEM). In this paper, we compare with available free surface velocity from Morrow *et al*. (2017a), and we further examine the material volume fractions of all components in the specimen in this paper by EBSD. The quantitative information in the distributions of temperature, strain, stress and volume fractions of components will be obtained during impact loading, which is not available experimentally.

This paper is organized as follows. The kinematics at large deformation is presented in Section 2. The thermodynamically consistent driving forces for plastic slip, twinning and phase

transformation are developed in Section 3. The constitutive equations for nonlinear elasticity, twinning, phase transformation, and dislocation slip are introduced in Sections 4, 5, 6 and 7, respectively. The evolution of temperature is presented in Section 8. Plate impact experiment, model, and material parameters are introduced in Section 9. Results obtained from FEM plate impact simulations on the high purity Ti are described and discussed in Section 10. Section 11 concludes this paper with remarks and additional observations.

Throughout this manuscript, vectors and tensors are written as boldface and non-italic symbols. Contractions of the second-order tensors $\mathbf{A}=\{A_{kl}\}$ and $\mathbf{B}=\{B_{mn}\}$ over one and two indices are designated as $\mathbf{A}\cdot\mathbf{B}=\{A_{kl}B_{lm}\}$ and $\mathbf{A}:\mathbf{B}=\{A_{kl}B_{lk}\}$, respectively. Similarly, we define contractions of the forth-order tensor $\underline{\mathbf{K}}$ and second-order tensor $\mathbf{B}$, over one and two indices as $\underline{\mathbf{K}}\cdot\mathbf{B}=\{K_{klmn}B_{ni}\}$ and $\underline{\mathbf{K}}:\mathbf{B}=\{K_{klmn}B_{nm}\}$.

2. Large deformation kinematics

The motion of a material under finite deformation is described by a continuous vector function $\mathbf{r}=\mathbf{r}(\mathbf{r}_0,t)$. Here, $\mathbf{r}$ and $\mathbf{r}_0$ are the position vectors of material points in the current (deformed) configuration Ω at the time instant t and in the reference (undeformed) configuration Ω_0 at the instant t_0, respectively. The deformation gradient $\mathbf{F}=\dfrac{\partial\mathbf{r}}{\partial\mathbf{r}_0}$ can be multiplicatively decomposed into elastic $\mathbf{F}_e$, plastic slip $\mathbf{F}_{sl}$, phase transformation $\mathbf{F}_{pt}$, and twinning $\mathbf{F}_{tw}$ contributions:

$$\mathbf{F}=\mathbf{F}_e\cdot\mathbf{F}_{sl}\cdot\mathbf{F}_{pt}\cdot\mathbf{F}_{tw}=\mathbf{R}_e\cdot\mathbf{U}_e\cdot\mathbf{F}_{sl}\cdot\mathbf{F}_{pt}\cdot\mathbf{F}_{tw};\qquad \mathbf{F}_e=\mathbf{R}_e\cdot\mathbf{U}_e \tag{1}$$

Here, $\mathbf{R}_e$ is the proper orthogonal rotation tensor and $\mathbf{U}_e$ is the symmetric elastic right stretch tensor. Fig. 1 graphically represents the decomposition of deformation gradient $\mathbf{F}$ in Eq. (1). Many times, dislocation slip $\mathbf{F}_{sl}$ and deformation twinning $\mathbf{F}_{tw}$ are considered in the same configuration in literature. For example, Kalidindi (1998) considered plastic slip and twinning in a combined way by the velocity gradient $\dot{\mathbf{F}}_p\cdot\mathbf{F}_p^{-1}$ in one unloaded intermediate configuration, where $\mathbf{F}_p$ is the plastic deformation gradient caused by both twinning and slip. Since slip and twinning describe two different physical behaviors, it is reasonable to consider them in two

configurations. In our model, plastic slip and twinning are considered separately: Ω_{sl} and Ω_{tw} in Fig. (1), and they are separated by an intermediate configuration Ω_{pt}. The sequence for each inelastic process is chosen in Eq. (1) for two reasons. First, the plastic slip in a configuration Ω_{sl} is after Ω_{pt} and Ω_{tw} because plastic slip is considered in both the α twinned variants and the ω variants, and it happens after the new α and ω variants are formed as shown in Fig. 1. Second, the configuration Ω_{pt} follows from Ω_{tw} because phase transformation in α twinned variants are considered and it takes place after α variants are generated. We acknowledge that other choices of the sequences among slip, phase transformation and twinning are possible and may have their own advantages. The sequence chosen here was not arbitrary but chosen due to both physical and numerical considerations. Here, we only emphasize that the four processes of elasticity, slip, twinning, and phase transformation are separated into four different configurations (Fig. 1), which is beneficial to derive the thermodynamic driving force for each process.

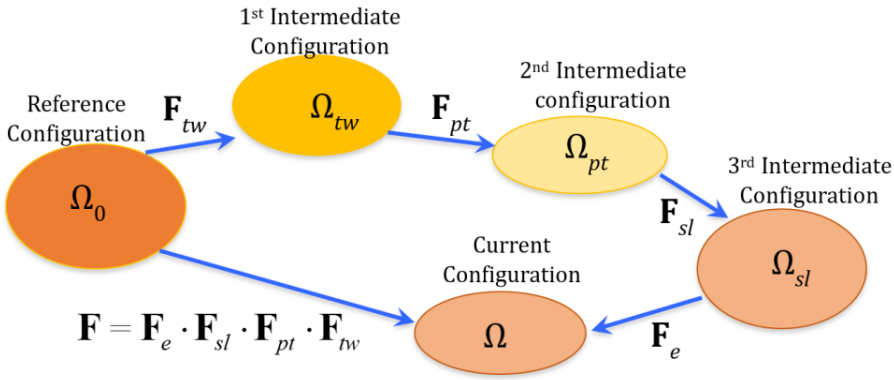

Fig. 1. Schematic of the decomposition of the deformation gradient $\mathbf{F}$. These are components of elasticity ($\mathbf{F}_e$), dislocation slip ($\mathbf{F}_{sl}$), phase transformation ($\mathbf{F}_{pt}$), and deformation twinning ($\mathbf{F}_{tw}$) defining the three intermediate configurations.

From Eq. (1), the time rate and inversion of the deformation gradient $\mathbf{F}$ are given by

$$\begin{aligned}\dot{\mathbf{F}} &= \dot{\mathbf{F}}_e\cdot\mathbf{F}_{sl}\cdot\mathbf{F}_{pt}\cdot\mathbf{F}_{tw}+\mathbf{F}_e\cdot\dot{\mathbf{F}}_{sl}\cdot\mathbf{F}_{pt}\cdot\mathbf{F}_{tw}+\mathbf{F}_e\cdot\mathbf{F}_{sl}\cdot\dot{\mathbf{F}}_{pt}\cdot\mathbf{F}_{tw}+\mathbf{F}_e\cdot\mathbf{F}_{sl}\cdot\mathbf{F}_{pt}\cdot\dot{\mathbf{F}}_{tw};\\ \mathbf{F}^{-1} &= \mathbf{F}_{tw}^{-1}\cdot\mathbf{F}_{pt}^{-1}\cdot\mathbf{F}_{sl}^{-1}\cdot\mathbf{F}_e^{-1}.\end{aligned} \tag{2}$$

The velocity gradient $\mathbf{L}=\dot{\mathbf{F}}\cdot\mathbf{F}^{-1}$ can be additively decomposed into the skew-symmetric spin tensor $\mathbf{W}=(\mathbf{L})_a$ and the symmetric stretching tensor $\mathbf{D}=(\mathbf{L})_s$; $\mathbf{L}=\mathbf{W}+\mathbf{D}$, in which the

subscripts *a* and *s* stand for skew-symmetric and symmetric forms of a tensor, respectively. From Eq. (2), $\mathbf{L}$ yields

$$\begin{aligned}\mathbf{L} = \dot{\mathbf{F}} \cdot \mathbf{F}^{-1} = \dot{\mathbf{F}}_e \cdot \mathbf{F}_e^{-1} + \mathbf{F}_e \cdot \dot{\mathbf{F}}_{sl} \cdot \mathbf{F}_{sl}^{-1} \cdot \mathbf{F}_e^{-1} + \mathbf{F}_e \cdot \mathbf{F}_{sl} \cdot \dot{\mathbf{F}}_{pt} \cdot \mathbf{F}_{pt}^{-1} \cdot \mathbf{F}_{sl}^{-1} \cdot \mathbf{F}_e^{-1} \\ + \mathbf{F}_e \cdot \mathbf{F}_{sl} \cdot \mathbf{F}_{pt} \cdot \dot{\mathbf{F}}_{tw} \cdot \mathbf{F}_{tw}^{-1} \cdot \mathbf{F}_{pt}^{-1} \cdot \mathbf{F}_{sl}^{-1} \cdot \mathbf{F}_e^{-1} = \mathbf{L}_e + \mathbf{L}_{sl} + \mathbf{L}_{pt} + \mathbf{L}_{tw}.\end{aligned} \tag{3}$$

The stress power in the current configuration $(\boldsymbol{\sigma} : \mathbf{D})$ is the double contraction of Cauchy stress $\boldsymbol{\sigma}$ and symmetric stretching tensor $\mathbf{D}$, and we have

$$\begin{aligned}\boldsymbol{\sigma} : \mathbf{D} = \boldsymbol{\sigma} : \mathbf{D} + \boldsymbol{\sigma} : \mathbf{W} = \boldsymbol{\sigma} : \mathbf{L} = \boldsymbol{\sigma} : \dot{\mathbf{F}}_e \cdot \mathbf{F}_e^{-1} + \boldsymbol{\sigma} : \mathbf{F}_e \cdot \dot{\mathbf{F}}_{sl} \cdot \mathbf{F}_{sl}^{-1} \cdot \mathbf{F}_e^{-1} + \\ \boldsymbol{\sigma} : \mathbf{F}_e \cdot \mathbf{F}_{sl} \cdot \dot{\mathbf{F}}_{pt} \cdot \mathbf{F}_{pt}^{-1} \cdot \mathbf{F}_{sl}^{-1} \cdot \mathbf{F}_e^{-1} + \boldsymbol{\sigma} : \mathbf{F}_e \cdot \mathbf{F}_{sl} \cdot \mathbf{F}_{pt} \cdot \dot{\mathbf{F}}_{tw} \cdot \mathbf{F}_{tw}^{-1} \cdot \mathbf{F}_{pt}^{-1} \cdot \mathbf{F}_{sl}^{-1} \cdot \mathbf{F}_e^{-1},\end{aligned} \tag{4}$$

in which the double contraction of a symmetric tensor and a skew-symmetric tensor is zero $(\boldsymbol{\sigma} : \mathbf{W} = 0)$. The Green-Lagrange elastic strain tensor $\mathbf{E}_e$ is chosen as our elastic strain measure:

$$\mathbf{E}_e = \frac{1}{2}\left(\mathbf{F}_e^T \cdot \mathbf{F}_e - \mathbf{I}\right) = \frac{1}{2}\left(\mathbf{U}_e \cdot \mathbf{U}_e - \mathbf{I}\right). \tag{5}$$

$\mathbf{E}_e$ is often used as elastic strain tensor for crystal materials since it excludes the lattice rotation $\mathbf{R}_e$ in the elastic process $\mathbf{F}_e$. The relation between $\mathbf{D}_e = \left(\dot{\mathbf{F}}_e \cdot \mathbf{F}_e^{-1}\right)_s$ and $\dot{\mathbf{E}}_e$ is as follows

$$\mathbf{D}_e = \left(\dot{\mathbf{F}}_e \cdot \mathbf{F}_e^{-1}\right)_s = \mathbf{F}_e^{-T} \cdot \dot{\mathbf{E}}_e \cdot \mathbf{F}_e^{-1}. \tag{6}$$

The derivation of Eq. (6) can be found in for example Levitas (1996) and Feng *et al*. (2018a).

The velocity gradient due to dislocation slip can be defined as

$$\dot{\mathbf{F}}_{sl} \cdot \mathbf{F}_{sl}^{-1} = \sum_i \sum_\beta c_i \dot{\gamma}_{\beta i-sl} \mathbf{s}_{\beta i} \otimes \mathbf{m}_{\beta i}, \qquad \dot{\gamma}_{\beta i-sl} = b_{\beta i} \rho_{M\beta i} v_{\beta i}. \tag{7}$$

In Eq. (7), slip rate $\dot{\gamma}_{\beta i-sl}$ is defined at the slip system β of the *i*-th component, where each variant of α and ω phase is called as one "component". In this paper, the subscripts β and η are used for different slip systems, and *i* and *j* stand for different components. There are fifteen slip systems in the α phase single crystal and six slip systems in the ω phase single crystal. Single crystal HCP Ti can be twinned into six possible compressive twin variants by compression along the *c*-axis of the lattice, and these six α phase twin variants may further transform into seven ω phase variants. The summation over index *i* in Eq. (7) is from *i*=0 to *i*=13, with *i*=0 representing the parent α material. For the α phase, *i* varies from 0 to 6 representing

the parent and six twin variants, while the summation of β is from 1 to 15 for fifteen slip systems. For the ω phase, i varies from 7 to 13, and the summation of β is from 1 to 6 for six slip systems. Symbols and numbers for material components and slip modes are presented in Table 1. In Eq. (7), the vector $\mathbf{s}_{\beta i}$ represents the slip direction, $\mathbf{m}_{\beta i}$ stands for the slip plane normal, c_i is the mass fraction or the volume fraction of the i-th component, Burgers vector is $b_{\beta i}$, and mobile dislocation density is $\rho_{M\beta i}$ with a mean velocity $v_{\beta i}$.

Components or slip modes (symbols)	Parent material (i or j)	Primary α twins (i or j)	ω components (i or j)	α Phase slip mode (β or η)	ω phase slip mode (β or η)
Number	0	1-6	7-13 (equals alpha component (0-6) plus 7)	1-15 (1-12 for pyramidal and 13-15 prismatic slip)	1-6

Table 1 Symbols and numbers for the material components and slip modes.

The velocity gradient due to deformation twinning is defined as

$$\dot{\mathbf{F}}_{tw} \cdot \mathbf{F}_{tw}^{-1} = \sum_{i} \dot{c}_{i-tw} \gamma_{tw} \mathbf{b}_i \otimes \mathbf{n}_i , \tag{8}$$

where the material parameter γ_{tw} is a shear strain magnitude caused by deformation twinning when the parent material fully transforms into one of the six possible α twin variants, the vector $\mathbf{b}_i$ represents the twinning direction and $\mathbf{n}_i$ stands for the twinning plane normal for the i-th compressive twin. For six compressive twins (i.e. primary twins), the summation of i is from 1 to 6. At any instant t, the concentration rate of the i-th compressive twin $\dot{c}_i$ can be composed into two contributions: $\dot{c}_i = \dot{c}_{i-tw} + \dot{c}_{i-pt}$, in which nonnegative $\dot{c}_{i-tw}$ is due to the parent α component twinned into the i-th twin and non-positive $\dot{c}_{i-pt}$ is caused by phase transformation from the i-th twin to ω phase. When the parent material transforms to the compressive twin phases, we have $\dot{c}_{0-tw} = -\sum_{i=1}^{6} \dot{c}_{i-tw}$, and when the α phase transforms to the ω phase, it yields $\dot{c}_{i-pt}\big|_{i=0 \text{ to } 6} = -\dot{c}_{j-pt}\big|_{j=i+7}$.

Transformational deformation gradient and its rate are defined as

$$\mathbf{F}_{pt} = \mathbf{I} + \sum_{i=7}^{13} c_i \, \boldsymbol{\varepsilon}_{i-pt}, \qquad \dot{\mathbf{F}}_{pt} = \sum_{i=7}^{13} \dot{c}_i \, \boldsymbol{\varepsilon}_{i-pt} . \tag{9}$$

In Eq. (9), the strain tensor $\boldsymbol{\varepsilon}_{i-pt}$ determines the transformational deformation of materials when the *i*-th $(i = j-7)$ α component completely transforms into the *j*-th ω component. The quantity $\dot{c}_i$ (or c_i) for the ω components in Eq. (9) is equal to or greater than zero because further transformation from the ω phase to other phases such as β phase only occurs at much higher temperature or pressure than the experiments and simulations considered in this study.

3. Application of the second law of thermodynamics

The second law of thermodynamics in the form of the Clausius-Duhem inequality in the current configuration Ω is

$$\rho D = \boldsymbol{\sigma} : \mathbf{D} - \rho \dot{\Psi} - \rho s \dot{\theta} - \frac{\nabla \theta}{\theta} \cdot \mathbf{h} \geq 0 . \tag{10}$$

Here, D is the dissipation rate per unit mass, ρ the mass density in the current configuration, Ψ the Helmholtz free energy (energy per unit mass), temperature θ, heat flux $\mathbf{h}$, and entropy s. The detailed derivation of Eq. (10) is presented in a number of continuum mechanics textbooks (e.g. Irgens, 2008; Clayton, 2010). As usual, we assume that the heat conduction due to the heat flux $\mathbf{h}$ is independent of other terms in Eq. (10). Then the inequality Eq. (10) transforms to two well-known inequalities: Planck's inequality and Fourier's inequality as written in Eq. (11):

$$\boldsymbol{\sigma} : \mathbf{D} - \rho \dot{\Psi} - \rho s \dot{\theta} \geq 0 ; \qquad -\frac{\nabla \theta}{\theta} \cdot \mathbf{h} \geq 0 . \tag{11}$$

$-\frac{\nabla \theta}{\theta} \cdot \mathbf{h} \geq 0$ means that heat input causes a temperature increase, which is satisfied by all known experiments. Therefore, we will only pay attention to the first inequality of Eq. (11). We introduce the specific Helmholtz free energy $\Psi\left(\mathbf{E}_e, \theta, c_1, ..., c_i, ..., c_{13}\right)$, in which the Green-Lagrange elastic strain $\mathbf{E}_e$ is defined in Eq. (5) and c_1 to c_{13} are volume fractions of all ω variants and compressive twins as in Table 1. Here c_0 for the parent material is not chosen as an independent variable for Helmholtz free energy Ψ and there are only thirteen independent

concentrations since $\sum_{i=0}^{13} c_i = 1$. Choosing any one among $c_i|_{i=0,\ldots,13}$ to be excluded from the independent variables of Ψ is arbitrary.

In a representative volume *V* with the elastic strain $\mathbf{E}_e$ and temperature θ, it is usually practiced in crystal mechanics (e.g. Bronkhorst et al., 1992; Kalidindi, 1998) that each component of material in this volume *V* is subjected to the same $\mathbf{E}_e$ and θ. We assume this here as well. Therefore, Helmholtz free energy can be further written as:

$$\Psi\left(\mathbf{E}_e, \theta, c_1, ..., c_i, ..., c_n\right) = \sum_{i=0}^{13} c_i \Psi_i\left(\mathbf{E}_e, \theta\right) \tag{12}$$

Here $\Psi_i\left(\mathbf{E}_e, \theta\right)$ is the Helmholtz free energy for the *i*-th component and the material constants in elasticity and the thermal potential are from the *i*-th component for $\Psi_i\left(\mathbf{E}_e, \theta\right)$. Further if c_0 is excluded from this expression, we have

$$\Psi = \sum_{i=0}^{13} c_i \Psi_i\left(\mathbf{E}_e, \theta\right) = \sum_{i=1}^{13} c_i \Psi_i\left(\mathbf{E}_e, \theta\right) + \left(1 - \sum_{i=1}^{13} c_i\right) \Psi_0\left(\mathbf{E}_e, \theta\right). \tag{13}$$

Combining Eqs. (4) and (6) into Eq. (11) and sorting terms, we can obtain

$$\begin{aligned}
&\boldsymbol{\sigma} : \mathbf{D} - \rho\dot{\Psi} - \rho s\dot{\theta} = (\boldsymbol{\sigma} : \dot{\mathbf{F}}_e \cdot \mathbf{F}_e^{-1} + \boldsymbol{\sigma} : \mathbf{F}_e \cdot \dot{\mathbf{F}}_{sl} \cdot \mathbf{F}_{sl}^{-1} \cdot \mathbf{F}_e^{-1} + \boldsymbol{\sigma} : \mathbf{F}_e \cdot \mathbf{F}_{sl} \cdot \dot{\mathbf{F}}_{pt} \cdot \mathbf{F}_{pt}^{-1} \cdot \mathbf{F}_{sl}^{-1} \cdot \mathbf{F}_e^{-1} \\
&+ \boldsymbol{\sigma} : \mathbf{F}_e \cdot \mathbf{F}_{sl} \cdot \mathbf{F}_{pt} \cdot \dot{\mathbf{F}}_{tw} \cdot \mathbf{F}_{tw}^{-1} \cdot \mathbf{F}_{pt}^{-1} \cdot \mathbf{F}_{sl}^{-1} \cdot \mathbf{F}_e^{-1}) - \rho\left(\frac{\partial \Psi}{\partial \mathbf{E}_e} : \dot{\mathbf{E}}_e + \frac{\partial \Psi}{\partial \theta}\dot{\theta} + \sum_{i=1}^{13} \frac{\partial \Psi}{\partial c_i}\dot{c}_i\right) - \rho s\dot{\theta} \\
&= \frac{\rho}{\tilde{\rho}}\left[\det \mathbf{F}_e \cdot \mathbf{F}_e^{-1} \cdot \boldsymbol{\sigma} \cdot \mathbf{F}_e^{-T} - \tilde{\rho}\frac{\partial \Psi}{\partial \mathbf{E}_e}\right] : \dot{\mathbf{E}}_e - \rho\left(\frac{\partial \Psi}{\partial \theta} + s\right)\dot{\theta} + \left(\boldsymbol{\sigma} : \mathbf{F}_e \cdot \dot{\mathbf{F}}_{sl} \cdot \mathbf{F}_{sl}^{-1} \cdot \mathbf{F}_e^{-1}\right) + \\
&\left(\boldsymbol{\sigma} : \mathbf{F}_e \cdot \mathbf{F}_{sl} \cdot \dot{\mathbf{F}}_{pt} \cdot \mathbf{F}_{pt}^{-1} \cdot \mathbf{F}_{sl}^{-1} \cdot \mathbf{F}_e^{-1} + \boldsymbol{\sigma} : \mathbf{F}_e \cdot \mathbf{F}_{sl} \cdot \mathbf{F}_{pt} \cdot \dot{\mathbf{F}}_{tw} \cdot \mathbf{F}_{tw}^{-1} \cdot \mathbf{F}_{pt}^{-1} \cdot \mathbf{F}_{sl}^{-1} \cdot \mathbf{F}_e^{-1} - \sum_{i=1}^{n} \rho \frac{\partial \Psi}{\partial c_i}\dot{c}_i\right) \geq 0.
\end{aligned} \tag{14}$$

Here, $\tilde{\rho}$ is the mass density in the configuration Ω_{sl} in Fig. 1. It is commonly accepted that the dissipation rate in Eq. (14) is independent of $\dot{\theta}$ and $\dot{\mathbf{E}}_e$, we can obtain the entropy function and the elasticity rule:

$$-\frac{\partial \Psi}{\partial \theta} = s; \qquad \det \mathbf{F}_e \cdot \mathbf{F}_e^{-1} \cdot \boldsymbol{\sigma} \cdot \mathbf{F}_e^{-T} - \tilde{\rho}\frac{\partial \Psi}{\partial \mathbf{E}_e} = 0 \Rightarrow \boldsymbol{\sigma} = \frac{1}{\det \mathbf{F}_e}\mathbf{F}_e \cdot \tilde{\rho}\frac{\partial \Psi}{\partial \mathbf{E}_e} \cdot \mathbf{F}_e^T. \tag{15}$$

Combining Eq. (15), Eq. (14) can be further transformed into

$$\boldsymbol{\sigma}:\mathbf{D}-\rho\dot{\Psi}-\rho s\dot{\theta}=\left(\boldsymbol{\sigma}:\mathbf{F}_e\cdot\dot{\mathbf{F}}_{sl}\cdot\mathbf{F}_{sl}^{-1}\cdot\mathbf{F}_e^{-1}\right)+$$
$$\left(\boldsymbol{\sigma}:\mathbf{F}_e\cdot\mathbf{F}_{sl}\cdot\dot{\mathbf{F}}_{pt}\cdot\mathbf{F}_{pt}^{-1}\cdot\mathbf{F}_{sl}^{-1}\cdot\mathbf{F}_e^{-1}+\boldsymbol{\sigma}:\mathbf{F}_e\cdot\mathbf{F}_{sl}\cdot\mathbf{F}_{pt}\cdot\dot{\mathbf{F}}_{tw}\cdot\mathbf{F}_{tw}^{-1}\cdot\mathbf{F}_{pt}^{-1}\cdot\mathbf{F}_{sl}^{-1}\cdot\mathbf{F}_e^{-1}-\sum_{i=1}^{n}\rho\frac{\partial\Psi}{\partial c_i}\dot{c}_i\right)\geq 0. \tag{16}$$

In Eq. (16), the term in the first parenthesis stands for dissipation rate due to plastic slip, and the term in the second parenthesis is for the combination of twinning and phase transformation. Since the plastic slip is a dissipative process (i.e. the dissipation rate due to plastic slip is non-negative), we have the following transformation by combining Eq. (7),

$$\begin{aligned}&\boldsymbol{\sigma}:\mathbf{F}_e\cdot\dot{\mathbf{F}}_{sl}\cdot\mathbf{F}_{sl}^{-1}\cdot\mathbf{F}_e^{-1}=\mathbf{F}_e^{-1}\cdot\boldsymbol{\sigma}\cdot\mathbf{F}_e:\dot{\mathbf{F}}_{sl}\cdot\mathbf{F}_{sl}^{-1}=\mathbf{F}_e^{-1}\cdot\boldsymbol{\sigma}\cdot\mathbf{F}_e:\sum_i\sum_\beta c_i\dot{\gamma}_{sl-\beta i}\mathbf{s}_{\beta i}\otimes\mathbf{m}_{\beta i}\\&=\sum_i\sum_\beta c_i\left[\mathbf{F}_e^{-1}\cdot\boldsymbol{\sigma}\cdot\mathbf{F}_e:\left(\mathbf{s}_{\beta i}\otimes\mathbf{m}_{\beta i}\right)\right]\dot{\gamma}_{sl-\beta i}=\sum_i\sum_\beta c_i\tau_{\beta i}\dot{\gamma}_{sl-\beta i}\geq 0;\end{aligned} \tag{17}$$

$$\tau_{\beta i}=\mathbf{F}_e^{-1}\cdot\boldsymbol{\sigma}\cdot\mathbf{F}_e:\left(\mathbf{s}_{\beta i}\otimes\mathbf{m}_{\beta i}\right). \tag{18}$$

In each slip system of each composition: $\left(\mathbf{s}_{\beta i},\mathbf{m}_{\beta i}\right)$, the plastic slip process is dissipative: $c_i\tau_{\beta i}\dot{\gamma}_{sl-\beta i}\geq 0$. Consequently $\tau_{\beta i}$ in Eq. (17) and $\dot{\gamma}_{sl-\beta i}$ should always have the same sign, which indicates that $\dot{\gamma}_{\beta i}$ must be a function of $\tau_{\beta i}$. This $\tau_{\beta i}$ as shown earlier, is obtained from a rigorous derivation of the second law of thermodynamics, serving as the driving force for plastic slip on system β in the *i*-th phase. In Section 7, we will find that Eq. (17) will always be satisfied.

Before developing the driving force for deformation twinning and phase transformation, we introduce the following transformation for $\sum_{i=1}^{13}\rho\frac{\partial\Psi}{\partial c_i}\dot{c}_i$ by combining Eq. (13):

$$\begin{aligned}&\sum_{i=1}^{13}\rho\frac{\partial\Psi}{\partial c_i}\dot{c}_i=\rho\sum_{i=1}^{13}\dot{c}_i\left(\Psi_i-\Psi_0\right)=\rho\sum_{i=1}^{6}\left(\dot{c}_{i-tw}+\dot{c}_{i-pt}\right)\left(\Psi_i-\Psi_0\right)+\rho\sum_{i=7}^{13}\dot{c}_{i-pt}\left(\Psi_i-\Psi_0\right)\\&=\rho\sum_{i=1}^{6}\dot{c}_{i-tw}\left(\Psi_i-\Psi_0\right)+\rho\sum_{i=1}^{13}\dot{c}_{i-pt}\Psi_i-\rho\sum_{i=1}^{13}\dot{c}_{i-pt}\Psi_0=\rho\sum_{i=1}^{6}\dot{c}_{i-tw}\left(\Psi_i-\Psi_0\right)+\rho\sum_{i=1}^{13}\dot{c}_{i-pt}\Psi_i-\rho\dot{c}_{7-pt}\Psi_0\\&=\rho\sum_{i=1}^{6}\dot{c}_{i-tw}\left(\Psi_i-\Psi_0\right)+\rho\sum_{i=0}^{13}\dot{c}_{i-pt}\Psi_i=\rho\sum_{i=1}^{6}\dot{c}_{i-tw}\left(\Psi_i-\dot{\Psi}_0\right)+\rho\sum_{i=7}^{13}\dot{c}_{i-pt}\left(\Psi_i-\Psi_{i-7}\right),\end{aligned} \tag{19}$$

where $\dot{c}_{i-pt}\big|_{i=0\text{ to }6}=-\dot{c}_{j-pt}\big|_{j=i+7}$ (i.e. the law of mass conservation) is used. For multicomponent systems with volume change during phase transformation, c_i means volume fraction in the reference configuration or the mass volume fraction, which is convenient to use for applying the law of mass conservation.

The twinning and phase transformation processes in the second parenthesis of Eq. (16) can be written separately by the following transformation,

$$\begin{aligned}
&\boldsymbol{\sigma}:\mathbf{F}_e\cdot\mathbf{F}_{sl}\cdot\dot{\mathbf{F}}_{pt}\cdot\mathbf{F}_{pt}^{-1}\cdot\mathbf{F}_{sl}^{-1}\cdot\mathbf{F}_e^{-1}+\boldsymbol{\sigma}:\mathbf{F}_e\cdot\mathbf{F}_{sl}\cdot\mathbf{F}_{pt}\cdot\dot{\mathbf{F}}_{tw}\cdot\mathbf{F}_{tw}^{-1}\cdot\mathbf{F}_{pt}^{-1}\cdot\mathbf{F}_{sl}^{-1}\cdot\mathbf{F}_e^{-1}-\sum_{i=1}^{n}\rho\frac{\partial\Psi}{\partial c_i}\dot{c}_i\\
&=\left[\boldsymbol{\sigma}:\mathbf{F}_e\cdot\mathbf{F}_{sl}\cdot\dot{\mathbf{F}}_{pt}\cdot\mathbf{F}_{pt}^{-1}\cdot\mathbf{F}_{sl}^{-1}\cdot\mathbf{F}_e^{-1}-\rho\sum_{i=7}^{13}\dot{c}_{i-pt}\left(\Psi_i-\Psi_{i-7}\right)\right]\\
&+\left[\boldsymbol{\sigma}:\mathbf{F}_e\cdot\mathbf{F}_{sl}\cdot\mathbf{F}_{pt}\cdot\dot{\mathbf{F}}_{tw}\cdot\mathbf{F}_{tw}^{-1}\cdot\mathbf{F}_{pt}^{-1}\cdot\mathbf{F}_{sl}^{-1}\cdot\mathbf{F}_e^{-1}-\rho\sum_{i=1}^{6}\dot{c}_{i-tw}\left(\Psi_i-\dot{\Psi}_0\right)\right].
\end{aligned}\tag{20}$$

Consequently, the dissipation rate caused by phase transformation from Eq. (20) is non-negative and yields,

$$\begin{aligned}
&\boldsymbol{\sigma}:\mathbf{F}_e\cdot\mathbf{F}_{sl}\cdot\dot{\mathbf{F}}_{pt}\cdot\mathbf{F}_{pt}^{-1}\cdot\mathbf{F}_{sl}^{-1}\cdot\mathbf{F}_e^{-1}-\rho\sum_{i=7}^{13}\dot{c}_{i-pt}\left(\Psi_i-\Psi_{i-7}\right)\\
&=\mathbf{F}_{pt}^{-1}\cdot\mathbf{F}_{sl}^{-1}\cdot\mathbf{F}_e^{-1}\cdot\boldsymbol{\sigma}\cdot\mathbf{F}_e\cdot\mathbf{F}_{sl}:\dot{\mathbf{F}}_{pt}-\rho\sum_{i=7}^{13}\dot{c}_{i-pt}\left(\Psi_i-\Psi_{i-7}\right)\\
&=\mathbf{F}_{pt}^{-1}\cdot\mathbf{F}_{sl}^{-1}\cdot\mathbf{F}_e^{-1}\cdot\boldsymbol{\sigma}\cdot\mathbf{F}_e\cdot\mathbf{F}_{sl}:\sum_{i=7}^{13}\dot{c}_{i-pt}\boldsymbol{\varepsilon}_{i-pt}-\rho\sum_{i=7}^{13}\dot{c}_{i-pt}\left(\Psi_i-\Psi_{i-7}\right)\\
&=\sum_{i=7}^{13}\left[\mathbf{F}_{pt}^{-1}\cdot\mathbf{F}_{sl}^{-1}\cdot\mathbf{F}_e^{-1}\cdot\boldsymbol{\sigma}\cdot\mathbf{F}_e\cdot\mathbf{F}_{sl}:\boldsymbol{\varepsilon}_{i-pt}-\rho\left(\Psi_i-\Psi_{i-7}\right)\right]\dot{c}_{i-pt}\geq 0.
\end{aligned}\tag{21}$$

where, the macroscopic driving force for each phase transformation is

$$X_{i-pt}=\mathbf{F}_{pt}^{-1}\cdot\mathbf{F}_{sl}^{-1}\cdot\mathbf{F}_e^{-1}\cdot\boldsymbol{\sigma}\cdot\mathbf{F}_e\cdot\mathbf{F}_{sl}:\boldsymbol{\varepsilon}_{i-pt}-\rho\left(\Psi_i-\Psi_{i-7}\right).\tag{22}$$

X_{i-pt} must have the same sign as $\dot{c}_{i-pt}$ to satisfy a non-negative dissipation for phase transformation from each α variant into corresponding ω variant in Eq. (21). Therefore, in Section 6, $\dot{c}_{i-pt}$ will be introduced as a function of X_{i-pt}, and hence the phase transformation in Eq. (21) is thermodynamically consistent.

From Eq. (20), the dissipation rate caused by deformation twinning obeys:

$$
\begin{aligned}
&\boldsymbol{\sigma}:\mathbf{F}_e\cdot\mathbf{F}_{sl}\cdot\mathbf{F}_{pt}\cdot\dot{\mathbf{F}}_{tw}\cdot\mathbf{F}_{tw}^{-1}\cdot\mathbf{F}_{pt}^{-1}\cdot\mathbf{F}_{sl}^{-1}\cdot\mathbf{F}_e^{-1}-\rho\sum_{i=1}^{6}\dot{c}_{i-tw}\left(\Psi_i-\dot{\Psi}_0\right)\\
&=\mathbf{F}_{pt}^{-1}\cdot\mathbf{F}_{sl}^{-1}\cdot\mathbf{F}_e^{-1}\cdot\boldsymbol{\sigma}\cdot\mathbf{F}_e\cdot\mathbf{F}_{sl}\cdot\mathbf{F}_{pt}:\dot{\mathbf{F}}_{tw}\cdot\mathbf{F}_{tw}^{-1}-\rho\sum_{i=1}^{6}\dot{c}_{i-tw}\left(\Psi_i-\Psi_0\right)\\
&=\mathbf{F}_{pt}^{-1}\cdot\mathbf{F}_{sl}^{-1}\cdot\mathbf{F}_e^{-1}\cdot\boldsymbol{\sigma}\cdot\mathbf{F}_e\cdot\mathbf{F}_{sl}\cdot\mathbf{F}_{pt}:\sum_{i=1}^{6}\dot{c}_{i-tw}\gamma_{tw}\mathbf{b}_i\otimes\mathbf{n}_i-\rho\sum_{i=1}^{6}\dot{c}_{i-tw}\left(\Psi_i-\Psi_0\right)\\
&=\sum_{i=1}^{6}\left[\mathbf{F}_{pt}^{-1}\cdot\mathbf{F}_{sl}^{-1}\cdot\mathbf{F}_e^{-1}\cdot\boldsymbol{\sigma}\cdot\mathbf{F}_e\cdot\mathbf{F}_{sl}\cdot\mathbf{F}_{pt}:\left(\mathbf{b}_i\otimes\mathbf{n}_i\right)\gamma_{tw}-\rho\left(\Psi_i-\Psi_0\right)\right]\dot{c}_{i-tw}\geq 0.
\end{aligned}
\tag{23}
$$

From Eq. (23), the macroscopic driving force for each compressive twin is

$$
X_{i-tw}=\mathbf{F}_{pt}^{-1}\cdot\mathbf{F}_{sl}^{-1}\cdot\mathbf{F}_e^{-1}\cdot\boldsymbol{\sigma}\cdot\mathbf{F}_e\cdot\mathbf{F}_{sl}\cdot\mathbf{F}_{pt}:\left(\mathbf{b}_i\otimes\mathbf{n}_i\right)\gamma_{tw}-\rho\left(\Psi_i-\Psi_0\right). \tag{24}
$$

Therefore, the driving force for both phase transformation and twinning has similar form so that the work done during the phase transformation or twinning process should overcome the change in Helmholtz free energy. In addition, for a Ti sample

$$
\mathbf{F}_{pt}^{-1}\cdot\mathbf{F}_{sl}^{-1}\cdot\mathbf{F}_e^{-1}\cdot\boldsymbol{\sigma}\cdot\mathbf{F}_e\cdot\mathbf{F}_{sl}\cdot\mathbf{F}_{pt}:\left(\mathbf{b}_i\otimes\mathbf{n}_i\right)\gamma_{tw}>>\rho\left(\Psi_i-\Psi_0\right), \tag{25}
$$

which is true for two reasons: first, the rotation of elastic stiffness matrix due to twinning is small, and second the elastic strain is much less than twinning strain (See details in Feng, *et al*., 2018a). Therefore, we can ignore the term $\rho\left(\Psi_i-\Psi_0\right)$ in the driving force X_{i-tw} in Eq. (24), and the evolution of $\dot{c}_{i-tw}$ must be a function of $X_{i-tw}\approx\mathbf{F}_{pt}^{-1}\cdot\mathbf{F}_{sl}^{-1}\cdot\mathbf{F}_e^{-1}\cdot\boldsymbol{\sigma}\cdot\mathbf{F}_e\cdot\mathbf{F}_{sl}\cdot\mathbf{F}_{pt}:\left(\mathbf{b}_i\otimes\mathbf{n}_i\right)\gamma_{tw}$. Since the quantity γ_{tw} is a positive material constant that does not affect the sign of X_{i-tw}, the concentration rate $\dot{c}_{i-tw}$ can be written as a function of the resolved shear stress

$$
\tau_{i-tw}=\mathbf{F}_{pt}^{-1}\cdot\mathbf{F}_{sl}^{-1}\cdot\mathbf{F}_e^{-1}\cdot\boldsymbol{\sigma}\cdot\mathbf{F}_e\cdot\mathbf{F}_{sl}\cdot\mathbf{F}_{pt}:\left(\mathbf{b}_i\otimes\mathbf{n}_i\right), \tag{26}
$$

which is the thermodynamically consistent driving force for the twinning process.

4. Nonlinear elasticity model

For single crystal Ti loaded by plate impact, the maximum temperature change is estimated to be 100 K. Since the thermal expansion coefficient for Ti is relatively small, the effects of thermal strain can be ignored. The Helmholtz free energy $\Psi\left(\mathbf{E}_e,c_1,...,c_n\right)=\sum_{i=0}^{13}c_i\Psi_i\left(\mathbf{E}_e\right)$ is considered as a function of the Green-Lagrange elastic strain

tensor $\mathbf{E}_e$ and volume fractions of all components, c_i. For small elastic deformation, the Helmholtz free energy can be defined as

$$\tilde{\rho}\Psi = \sum_{i=0}^{13} c_i \tilde{\rho}\Psi_i\left(\mathbf{E}_e\right) = \sum_{i=0}^{13} c_i \left(\frac{1}{2}\mathbf{E}_e : \mathbf{C}_i : \mathbf{E}_e\right); \qquad \tilde{\rho}\Psi_i\left(\mathbf{E}_e\right) = \frac{1}{2}\mathbf{E}_e : \mathbf{C}_i : \mathbf{E}_e, \tag{27}$$

where the material parameter $\mathbf{C}_i$ is the fourth-order elastic stiffness tensor of the *i*-th component. For a high-order-strain constitutive model for large elastic deformation, $\mathbf{C}_i$ is not constant but depends on $\mathbf{E}_e$. For example, under several megabar pressure, the high-order elastic strain theory for single crystal diamond is considered in Feng and Levitas (2017a,b) and Feng *et al*. (2016).

The lattice rotation due to twinning in the α phase with respect to the parent material is introduced by a rotation tensor $\mathbf{R}_i$ as in Kalidindi (1998),

$$\mathbf{R}_i = 2\mathbf{n}_i \otimes \mathbf{n}_i - \mathbf{I}, \tag{28}$$

in which the unit vector $\mathbf{n}_i$ is the twinning plane normal.

Let the elastic stiffness tensor for the parent α phase material be $\mathbf{C}_0 = C_{0-lmjk}\mathbf{e}_l\mathbf{e}_m\mathbf{e}_j\mathbf{e}_k$ in the base system of $\mathbf{e}_l\mathbf{e}_m\mathbf{e}_j\mathbf{e}_k$. Consequently, the stiffness $\mathbf{C}_i$ for the *i*-th compressive twin (Kalidindi, 1998) can be obtained from

$$\mathbf{C}_i = C_{0-lmjk}\left(\mathbf{R}_i \cdot \mathbf{e}_l\right)\left(\mathbf{R}_i \cdot \mathbf{e}_m\right)\left(\mathbf{R}_i \cdot \mathbf{e}_j\right)\left(\mathbf{R}_i \cdot \mathbf{e}_k\right). \tag{29}$$

By molecular dynamics simulation, Zong *et al*. (2014) found that experimentally observed lattice rotation between α and ω phase is caused by deformation twinning in the α phase as a pre-cursor to phase transformation, while phase transformation itself does not contain salient lattice rotation. This is also consistent with experimental evidence from pole figures experiments as shown below in the results section, where the lattice rotation is small between the α component and its corresponding ω component. Here we also hypothesize that there is no lattice rotation during phase transformation. Therefore, the stiffness of the ω component can be written as

$$\mathbf{C}_j = C_{7-lmjk}\left(\mathbf{R}_i \cdot \mathbf{e}_l\right)\left(\mathbf{R}_i \cdot \mathbf{e}_m\right)\left(\mathbf{R}_i \cdot \mathbf{e}_j\right)\left(\mathbf{R}_i \cdot \mathbf{e}_k\right); \qquad j = i + 6; \qquad i = 1, ..., 6\ . \tag{30}$$

Combining the elasticity rule in Eq. (15) and free energy expression in Eq. (27), Cauchy stress in the current configuration Ω and the second Piola-Kirchhoff stress $\mathbf{T}$ in the configuration Ω_{sl} yield

$$\boldsymbol{\sigma} = \frac{1}{\det \mathbf{F}_e} \mathbf{F}_e \cdot \tilde{\rho} \frac{\partial \Psi}{\partial \mathbf{E}_e} \cdot \mathbf{F}_e^T = \frac{1}{\det \mathbf{F}_e} \mathbf{F}_e \cdot \sum_{i=0}^{13} c_i \left(\mathbf{C}_i : \mathbf{E}_e \right) \cdot \mathbf{F}_e^T = \frac{1}{\det \mathbf{F}_e} \mathbf{F}_e \cdot \sum_{i=0}^{13} c_i \mathbf{T}_i \cdot \mathbf{F}_e^T . \tag{31}$$

Elastic constants	C_{11}, C_{22}	C_{33} (c-axis)	C_{12}, C_{13}, C_{23}	C_{44}, C_{55}, C_{66}
For α phase (GPa)	177.59	191.34	87.57	46.7
For ω phase (GPa)	190.4	205.1	93.8	50

Table 2. Values of elastic stiffness for Ti when the 3 coordinate axis is along the *c*-axis of the crystal lattice. (Fisher and Renken, 1964; Vohra, 1978).

The elasticity rule in Eq. (27) is based on small elastic strain theory. At large elastic strain it may fail because the high order elastic strain terms in the Helmholtz free energy given by Eq. (24) may also play a role (see an example on Helmholtz free energy with high order elastic strain terms for crystal elasticity and isotropic elasticity rules in Feng *et al*. (2016)). However, the deviatoric part of the Cauchy stress in Eq. (27), $\left(\frac{1}{\det \mathbf{F}_e} \mathbf{F}_e \cdot \left(\mathbf{C} : \mathbf{E}_e \right) \cdot \mathbf{F}_e^T \right)_{dev}$ can be accepted for the materials in which the plastic deformation can easily occur and elastic constants are not small. Specifically, in the case of HCP Ti and Zr, the deformation due to plastic slip and twinning occupy most of the deviatoric strain tensor and thus the deviatoric part of the elastic strain tensor is very small. This is the case for isotropic polycrystalline Ti and Zr, and for example, using the J_2 flow rule the deviatoric stress tensor is controlled by a small yield strength of the material (Feng and Levitas, 2017c). A small yield strength means small deviators of stress and elastic strain tensors, since the elastic constants are not small for Ti and Zr (Feng and Levitas, 2017c). Large elastic strain in HCP Ti and Zr can only be the volumetric elastic strain because the plastic slip and twinning are volume preserving processes. The volumetric part of the Cauchy stress, i.e. pressure, may increase up to a large value. The volumetric part of the Cauchy stress $-p\mathbf{I}$ is primarily from the second Piola-Kirchhoff stress $\left(\mathbf{C} : \mathbf{E}_e \right)_v$, and such a linear

relation between strain and stress is unable to represent shock conditions when pressure is high and the thermodynamics of non-infinitesimal compression is important. The pressure p_{eos} from the nonlinear equation of state (EOS) from Greeff *et al*. (2001) gives an excellent correspondence with experiments for Ti at pressure up to 80 GPa. The EOS has been constructed by developing a parametrized Helmholtz free energy (per unit mass in the current configuration Ω) as a function of specific volume v (volume per unit mass) and temperature θ at Ω,

$$\psi_{eos} = \psi_0(v) + \psi_{el}(v,\theta) + \psi_{vib}(v,\theta). \tag{32}$$

Here, $\psi_0(v)$, $\psi_{el}(v,\theta)$, and $\psi_{vib}(v,\theta)$ represent the static lattice potential, electronic excitation energy, and ion motion free energies, respectively. Pressure is largely controlled by the static lattice potential $\psi_0(v)$, and temperature is largely determined by ion motion $\psi_{vib}(v,\theta)$. The electronic excitation term $\psi_{el}(v,\theta)$ plays a small role on the pressure but is important for the entropy. Further we summarize their analytical expression in Greeff *et al*. (2001) as follows.

The static lattice potential $\psi_0(v)$ is defined as

$$\psi_0(v) = \psi^* + \frac{4v^*B^*}{\left(B_1^*-1\right)^2}\left[1-\left(1+\eta\right)e^{-\eta}\right]; \quad \eta = \frac{3}{2}\left[\left(\frac{v}{v^*}\right)^{1/3}-1\right]\left(B_1^*-1\right). \tag{33}$$

The electronic excitation free energy ψ_{el} is designated as

$$\psi_{el}(v,\theta) = -\frac{1}{2}\Gamma_0\left(\frac{v}{v_0}\right)^{\kappa}\theta^2. \tag{34}$$

The lattice vibrational free energy ψ_{vib} is expressed as

$$\psi_{vib}(v,\theta) = 2R\theta\left[\frac{1}{40}\left(\frac{\theta_2(v)}{\theta}\right)^2 - \ln\left(\frac{\theta}{\theta_0(v)}\right)\right], \quad \left(\theta_0(v) = \theta_0^*\, e^{-\frac{\gamma_0}{v_0}(v-v_0)};\ \theta_2(v) = \theta_0(v)\, e^{1/3}\right). \tag{35}$$

In Eqs. (33)-(35), B^* and B_1^* represent the bulk modulus and its pressure derivative respectively, v^* is the equilibrium volume, ψ^* controls the relative free energy of the two phases, v_0 is a specific volume at zero pressure, θ_0^* is the moment of the phonon spectrum, and all these material parameters including $R, \Gamma_0, \kappa,$ and γ_0 in Eqs. (33)-(35) are listed in Table 3 from Greeff

et al. (2001). Note that this form of the Helmhotz free energy does not employ the entire stress tensor although it is a very important capability to pursue in future development work. The Cauchy stress with EOS pressure representation for homogeneous single-phase materials is obtained from

$$\boldsymbol{\sigma} = \left(\frac{1}{\det \mathbf{F}_e} \cdot \mathbf{F}_e \cdot \left(\mathbf{C} : \mathbf{E}_e \right) \cdot \mathbf{F}_e^t \right)_{dev} - p_{eos} \mathbf{I}, \qquad \left(p_{eos} = -\frac{\partial \psi_{eos}}{\partial v} \right). \tag{36}$$

For heterogeneous materials with the combined α and ω system, we propose the following expression for pressure

$$p_{eos} = \sum_{i=0}^{6} c_i p_{eos-\alpha} + \sum_{i=7}^{13} c_i p_{eos-\omega}, \tag{37}$$

in which $p_{eos-\alpha}$ and $p_{eos-\varpi}$ is the pressure from EOS by using Eqs. (32) - (36) for the α and ω phases. Since the material parameters for α and ω phases are given in Table 3 and if we know the current specific volume v for both α and ω phases, $p_{eos-\alpha}$ and $p_{eos-\omega}$ in Eq. (37) will be easily obtained. As discussed before, we assume that all components are subjected to the same elastic deformation $\mathbf{E}_e$, and therefore $\det \mathbf{F}_e$ will also be the same for all phases due to the following relations:

$$\det \mathbf{F}_e = \left(\det \mathbf{F}_e \det \mathbf{F}_e^T \right)^{0.5} = \left[\det \left(\mathbf{F}_e \cdot \mathbf{F}_e^T \right) \right]^{0.5} = \left[\det \left(\mathbf{I} + 2\mathbf{E}_e \right) \right]^{0.5}. \tag{38}$$

The current specific volume for either α or ω phase can be calculated from

$$v = v_0 \det \mathbf{F}_e. \tag{39}$$

where v_0 is the specific volume from the α or ω phase when the load is zero (as listed in Table 3).

The difference between our formulation of the volumetric component of stress and that from the work of Luscher *et al*. (2017, 2018) is that they introduce $\left(\mathbf{F}_e^T \cdot \mathbf{F}_e \right)^{-1} p_{eos} \det \mathbf{F}_e$ into the volumetric part of the second Piola-Kirchhoff stress $\mathbf{T}$. Due to the term $\left(\mathbf{F}_e^T \cdot \mathbf{F}_e \right)^{-1}$, $\left(\mathbf{F}_e^T \cdot \mathbf{F}_e \right)^{-1} p_{eos} \det \mathbf{F}_e$ may be not completely volumetric and have deviatoric components. In addition, this paper considers the existence of multiple α and ω variants, instead of slip only within one component of material as in Luscher *et al*. (2017, 2018).

Quantity (unit)	ν_0 (m^3/kg)	γ_0 (1)	G_0 (J/(kg K^2))	θ_0 (K)	K (1)	v^* (m^3/g)	B^* (Pa)	B_1^* (1)	R (J/(kg K))	ψ^* (J/kg)
α phase	2.2194e-4	1.17	9.60334 e-2	252.0	1.45	2.2015 e-4	1.1008e11	4.3	173.699	0
ω phase	2.1837e-4	1.65	9.29019e-2	263.4	1.40	2.1608 e-4	1.1800e11	3.05	173.699	-1.5e4

Table 3. Values of Helmholtz free energy quantities for both Ti α and ω phases as taken from the work of Greeff *et al*. (2001).

5. Deformation twinning model

The model for deformation twinning in single crystal HCP Ti is developed based on the theory in Salem *et al*. (2005), where the rate of volume fractions for twinned HCP Ti varies by a power law of the resolved shear stress. In Section 3, the thermodynamically consistent resolved shear stress for the $(\mathbf{b}_i, \mathbf{n}_i)$ twin system is $\tau_{i-tw} = \mathbf{F}_{pt}^{-1} \cdot \mathbf{F}_{sl}^{-1} \cdot \mathbf{F}_e^{-1} \cdot \boldsymbol{\sigma} \cdot \mathbf{F}_e \cdot \mathbf{F}_{sl} \cdot \mathbf{F}_{pt} : (\mathbf{b}_i \otimes \mathbf{n}_i)$. From the results shown in Section 3, in order that the twinning process remains dissipative, the expression $\tau_{i-tw} \dot{c}_{i-tw} \geq 0$ must be satisfied; which indicates that $\dot{c}_{i-tw}$ must be a direct function of τ_{i-tw} and that the two quantities have the same sign. Here $\dot{c}_{i-tw}\big|_{i=1,2,...,6}$ is the time rate of mass fraction change of compressive twin variants during twinning. In this work the time rate of change of twin mass fractions is always non-negative because the compressive twins increase during loading. Further, based on Salem *et al*. (2005), the evolution of twin concentration is defined as,

$$\dot{c}_{i-tw}\big|_{i=1,2,...,6} = \begin{cases} 0 & \text{if } \tau_{tw-i} < \tau_{tw0} \\ \left(1 - \sum_{j=7}^{13} c_j\right)\left(1 - c_i^{b_0}\right) \dfrac{\dot{\gamma}_0}{\gamma_{tw}} \left(\dfrac{\tau_{tw-i}}{S_{tw}}\right)^{d_0} & \text{if } \tau_{tw-i} \geq \tau_{tw0} \end{cases}. \tag{40}$$

Here, positive valued τ_{tw0} is the magnitude of shear stress that must be overcome to initiate twinning, and it can be affected by the plastic deformation. The dislocations are densely piled up against the obstacles during plastic deformation, which generates a strong concentrator of the stress tensor and can reduce τ_{tw0} (Levitas, 2004; Feng and Levitas, 2017a; Levitas and

Javanbakht, 2015). In Eq. (40), the quantity $\dot{\gamma}_0$ is the reference shear rate and reference stress S_{tw} with the initial value S_{tw0} and evolves by

$$\dot{S}_{tw} = h_{tw}\left(\sum_i \gamma_{tw}\dot{c}_i\right)\left(\sum_i c_i\right)^{e_0} + h_{sl}\left(\sum_j\sum_\beta c_j\dot{\gamma}_{\beta j-sl}\right)\left(\sum_j\sum_\beta c_j\gamma_{\beta j-sl}\right)^{g_0}. \quad (41)$$

Here, $\left(\sum_i \gamma_{tw}\dot{c}_i\right)$ represents the equivalent shear rate of the *i*-th twin system; the summation of *i* is from 1 to the number of twinned variants 6; $\sum_j\sum_\beta c_j\gamma_{\beta j-sl}$ denotes the total shear strain due to plastic slip of both untwinned and twinned regions ($\gamma_{\beta j-sl}$ is from Eq. (7)), and *j* starts from 0 to the number of twinned systems 6. In addition, h_{tw}, e_0, d, h_{sl} and g_0 in Eq. (41) are material parameters. There are three main differences between Eqs. (40) and (41) and the model introduced by Salem *et al*. (2005). First, we introduced τ_{tw0} to consider the athermal dissipation during twinning mostly related to interface friction during twin-twin interface movement and the increase of surface energy during twinned area growing, and also to overcome the obstacles caused by dislocations and TSFs. Secondly, the *ω* phase acts as an effective matrix material since it does not deform by deformation twinning so we introduce $\left(1-\sum_{j=7}^{13} c_j\right)$ in Eq. (40). In Salem *et al*. (2005), $\left(1-\sum_{j=7}^{13} c_j\right)$ is equal to 1 since phase transformation is not considered. Third, our theory for twinning is formulated to be thermodynamically consistent. We also note that twinning is not included as a deformation mechanism for ω phase in this model since it was not observed in prior experimental results (Cerreta *et al*., 2005, 2006a,b).

6. Phase transformation model

In this work we use the transformation pathway suggested from both atomistic simulation (Zong *et al*., 2014) and experiment (Morrow *et al*. 2017a) under high strain rate loading, where phase transformation occurs on the twinned material and twinning causes the large rotation between the α and ω transition. Phase transformation within the parent material was not observed to be

present experimentally (Morrow *et al*., 2017a). It may be that the parent material contains a greater density of turbostratic stacking faults (TSFs) and since phase transformation pressure increases with increasing TSFs, the resistance to phase transformation is larger in the parent material (Levitas *et al*., 2016). As we will see from presented results, the amount of plastic slip in the twinned material is usually not as large as that in the parent material, especially for the case when the volume fraction of twinned material is much lower than the parent material as we have found here. While the phase transformation in the parent material does not take place under the loading conditions considered in the current paper, in Section 2-8 we include the phase transformation in both parent material and primary twins because if the loading is increased phase transformation can occur in parent material as well.

As we discussed in Section 3, the driving force for phase transformation $X_{i-pt} = \mathbf{F}_{pt}^{-1}\cdot\mathbf{F}_{sl}^{-1}\cdot\mathbf{F}_{e}^{-1}\cdot\boldsymbol{\sigma}\cdot\mathbf{F}_{e}\cdot\mathbf{F}_{sl} : \boldsymbol{\varepsilon}_{i-pt} - \rho\left(\Psi_i - \Psi_{i-7}\right)$: the work done during plastic slip overcomes the change in the Helmholtz free energy. In this paper, we consider the volumetric part of transformation strain, and formulated as done previously by Feng and Levitas, (2017c, 2018b). If the volumetric transformational strain is ε_{v-pt}, we have $\boldsymbol{\varepsilon}_{i-pt} = \varepsilon_{v-pt}\mathbf{I}/3$. In the current model, the major part of Helmholtz free energy is due to the volumetric deformation with high pressure. The deviatoric part of strain and stress are small and $\Psi_i - \Psi_{i-7} \approx \left(\psi_{eos-\varpi} - \psi_{eos-\alpha}\right)$, which is also accepted in Greeff *et al*. (2001) and in Addessio *et al*. (2017). Thus, the driving force for phase transformation in this paper is

$$X_{i-pt} \approx \mathbf{F}_{pt}^{-1}\cdot\mathbf{F}_{sl}^{-1}\cdot\mathbf{F}_{e}^{-1}\cdot\boldsymbol{\sigma}\cdot\mathbf{F}_{e}\cdot\mathbf{F}_{sl} : \boldsymbol{\varepsilon}_{i-pt} - \rho\left(\psi_{eos-\omega} - \psi_{eos-\alpha}\right) \tag{42}$$

We accept an exponential law suggested in Greeff *et al*. (2001) for rate of change of phase volume fraction:

$$\dot{c}_{i-pt} = \left[1-\left(c_{i-pt}\right)^{p_1}\right] w \frac{X_{i-pt}}{\beta_{tr}} \exp\left\{\left(\frac{X_{i-pt}}{\beta_{tr}}\right)^{q_1}\right\}, \tag{43}$$

where w and β_{tr} are the kinetic parameters that control phase transformation rate. Let us compare the driving force in this paper and the one in Greeff *et al*. (2001). Assuming that deformation in each process in Fig. 1 is small, then we have

$$X_{i-pt}=\mathbf{F}_{pt}^{-1}\cdot\mathbf{F}_{sl}^{-1}\cdot\mathbf{F}_{e}^{-1}\cdot\boldsymbol{\sigma}\cdot\mathbf{F}_{e}\cdot\mathbf{F}_{sl}:\boldsymbol{\varepsilon}_{i-pt}-\rho\left(\psi_{eos-\varpi}-\psi_{eos-\alpha}\right)\approx\boldsymbol{\sigma}:\boldsymbol{\varepsilon}_{i-pt}-\rho\left(\psi_{eos-\varpi}-\psi_{eos-\alpha}\right)$$
$$\approx p\varepsilon_{v-pt}-\rho\left(\psi_{eos-\varpi}-\psi_{eos-\alpha}\right)\approx\left[p\frac{v_2-v_1}{v_1}-\left(\psi_{eos-\varpi}-\psi_{eos-\alpha}\right)\right]\approx\rho_0\left[p\left(v_2-v_1\right)-\left(\psi_{eos-\varpi}-\psi_{eos-\alpha}\right)\right]. \tag{44}$$

In Greeff *et al*. (2001), the driving force as $X_{i-pt}=p\left(v_2-v_1\right)-\left(\psi_{eos-\varpi}-\psi_{eos-\alpha}\right)$ is equivalent with our model when deformation is small. The formulation proposed here extends that of Greeff *et al*. (2001) to large deformation. Barton *et al*. (2005) also considered phase transformation under conditions of large deformation and derived a driving force for these conditions.

7. Dislocation-based crystal plasticity model

In this section, we will propose a thermodynamically consistent dislocation based viscoplasticity model for multicomponent heterogeneous materials. In each slip system of each component: $\left(\mathbf{s}_{\beta i},\mathbf{m}_{\beta i}\right)$, the plastic slip process is dissipative: $c_i\tau_{\beta i}\dot{\gamma}_{sl-\beta i}\geq 0$, therefore, the slip rate $\dot{\gamma}_{sl-\beta i}$ and shear stress $\tau_{\beta i}$ must have the same sign all the time. The slip rate for a specific slip system and total slip rate for all slip systems can be written as

$$\dot{\gamma}_{\beta i}=b_{\beta i}\rho_{M\beta i}v_{\beta i};\quad \dot{\mathbf{F}}_{sl}\cdot\mathbf{F}_{sl}^{-1}=\sum_i\sum_\beta c_i\dot{\gamma}_{\beta i}\left(\mathbf{s}_{\alpha i}\otimes\mathbf{m}_{\alpha i}\right), \tag{45}$$

where $v_{\beta i}$ is the average dislocation velocity on slip system β and $\rho_{M\beta i}$ is the mobile dislocation density inside the *i*-th component. The real mobile dislocation density is averaged over a representative volume as $N_{M\beta i}=c_i\rho_{M\beta i}$. The velocity $v_{\beta i}$ is the only quantity to determine the sign of $\dot{\gamma}_{\beta i}$, which can be written as (e.g. Luscher *et al*., 2017)

$$v_{\beta i}=\frac{\tau_{\beta i}b_{\beta i}}{B_{\beta i}},\qquad B_{\beta i}=\frac{B_0}{1-\left(v_{\beta i}/c_s\right)^2}, \tag{46}$$

where $b_{\beta i}$ is the magnitude of the Burgers vector for slip system β of the *i*-th component; $B_{\beta i}$ is the viscous drag coefficient that increases without bound as $v_{\beta i}$ approaches the shear wave speed, c_s in the absence of relativistic effects; B_0 is the drag coefficient at zero velocity $v_{\beta i}$. The resolved shear stress $\tau_{\beta i}=\mathbf{F}_e^{-1}\cdot\boldsymbol{\sigma}\cdot\mathbf{F}_e:\left(\mathbf{s}_{\beta i}\otimes\mathbf{m}_{\beta i}\right)$ is for plastic slip (see its definition in Eq.

(18)), which is the only term in Eq. (46) determining the sign of $v_{\beta i}$ as positive, negative or zero. Consequently, $c_i\tau_{\beta i}\dot{\gamma}_{sl-\beta i} \geq 0$ is always satisfied and the plastic slip process is thermodynamically consistent.

Let us discuss the rotation of Schmid tensor of the parent material, α primary twins, and ω component. The orientation of the Schmid tensor for slip $\mathbf{s}_{\beta i} \otimes \mathbf{m}_{\beta i}$ in twin α variants is rotated together with the rotation of the crystal lattice by the following relationship (Kalidindi, 1998):

$$\mathbf{s}_{\beta i} \otimes \mathbf{m}_{\beta i} = \mathbf{R}_i \cdot \left(\mathbf{s}_{\beta 0} \otimes \mathbf{m}_{\beta 0}\right) \cdot \mathbf{R}_i^T, \tag{47}$$

where the rotation tensor $\mathbf{R}_i$ is from Eq. (28) and $\mathbf{s}_{\beta 0} \otimes \mathbf{m}_{\beta 0}$ is the Schmid tensor of the parent material. Since phase transformation does not change the lattice orientation for the Ti material considered here, the ω variant transformed from the *i*-th twinned HCP component follows the same rotation relationship with Eq. (47), in which $\mathbf{s}_{\beta 0} \otimes \mathbf{m}_{\beta 0}$ is the Schmid tensor of the hexagonal ω phase variant with the a_1 and c axes the same with the parent material, and $\mathbf{R}_i$ is still the rotation tensor in Eq. (28). An advanced theory for plastic slip is proposed in this paper based on the single crystal plasticity theory in Hansen *et al*. (2013) and multi-variant materials in Feng *et al*. (2018a). Here it is applied to the multiphase and multi-variant materials and the interactions among dislocations in different slip systems.

Three dislocation populations are considered in this paper as in Feng *et al*. (2018a) and Hansen *et al*. (2013); (1) mobile dislocations (subscript *M*) which is the only population having appreciable velocity, (2) pileup dislocations (subscript *P*) which are generated during pileup of mobile dislocations and are able to become mobile again if they escape from the temporary sessile state, and (3) locked sessile dislocations (subscript *L*) which do not belong to any slip system and are created when the mobile dislocations form locks and become sessile.

7.1 Dislocation interactions

The subscripts used in this section are defined as follows: η and β represent slip systems, *A* and *B* stand for the dislocation types (*M* or *P*), and *i* and *j* are for the different components such as any twin variants and ω variants. The interaction of any two dislocation slip systems $N_{A\eta i}$ and $N_{B\beta j}$ is discussed in this section, and when the type of dislocation is different

(i.e. *M* and *P*), the interactions considered here can take place in the same slip system (i.e. ηi and βj are the same) as well. From Hansen *et al*. (2013), the change rate $\dot{N}^{inter}_{A\eta i-B\beta j}$ of the dislocation density $N_{A\eta i}$ of the *i*-th component for the type *A* in the slip system η during the interaction with $N_{B\beta j}$ can be written as

$$\dot{N}^{inter}_{A\eta i-B\beta j} = P^{inter}_{A\eta i-B\beta j} D^{inter}_{A\eta i-B\beta j} f^{inter}_{A\eta i-B\beta j} N_{A\eta i} N_{B\beta j} \left| \boldsymbol{v}_{A\eta i-B\beta j} \right|. \quad (48)$$

The rate $\dot{N}^{inter}_{A\eta i-B\beta j}$ indicates that the dislocation density $N_{A\eta i}$ changes from one type into another type (i.e. from M to L, from M to P, from P to M, etc.). $\left| \boldsymbol{v}_{A\eta i-B\beta j} \right|$ is the absolute value of the relative velocity of dislocations of these two slip systems. $D^{inter}_{A\eta i-B\beta j}$ is the distance within which the interactions between $N_{A\eta i}$ and $N_{B\beta j}$ can occur. The term $f^{inter}_{A\eta i-B\beta j}$ is the fraction of dislocation density $N_{A\alpha i}$ that interacts with $N_{B\beta j}$ and changes the dislocation type. Annihilation only takes place between two dislocations having opposite Burgers vectors, and thus they mostly occur within the same slip systems while in the collinear slip systems the possibility is much rarer. As in Feng *et al*. (2018a), a fraction of $f^{inter}_{A\eta i-B\beta j}$, 0.25 is accepted for both annihilation and pileup when they occur in the same slip system (i.e. ηi and βj are the same); when $N_{A\alpha i}$ annihilates with or piles up on two different slip system, a fraction of 0.125 is used. In addition, the sessile locks are assumed to form during interactions at a fraction $f^{L}_{A\alpha i-B\beta j}$. All slip systems are assumed as equally likely to free a pileup dislocation, and thus for the escape of $N_{P\eta i}$, we have $f^{esc}_{P\eta i-M\beta j} = f^{esc}$, where $N_{P\eta i}$ must interact with a mobile dislocation $N_{M\beta j}$ to escape due to nonzero relative velocity in Eq. (48). The thermal probability $P^{inter}_{A\alpha i}$ is introduced due to the thermal barrier for the occurrence of an interaction. Attraction takes place between two dislocations with opposite Burgers vectors and annihilation always minimizes energy, which cause $P^{Anni}_{A\eta i} = 1$. The trapping of mobile dislocations becoming pileup dislocations and the escape of pileup dislocations are treated as thermally activated processes, and are governed by an Arrhenius equation as follows:

$$P_{A\eta i}^{trap} = e^{-esc} = e^{\left(\frac{\left(\left(\tau_{\eta i}^{G}-\left|\tau_{\eta i}\right|\right)b_{\eta i}{}^{2}-K_{A\eta i}\right)L}{k_b\theta}\right)} \quad \text{and} \quad P_{A\eta i}^{esc} = e^{esc} = e^{\left(\frac{-\left(\left(\tau_{\eta i}^{G}-\left|\tau_{\eta i}\right|\right)b_{\eta i}{}^{2}-K_{A\eta i}\right)L}{k_b\theta}\right)}. \tag{49}$$

In Eq. (49), θ and k_b stand for temperature and the Boltzmann's constant, respectively; $K_{A\eta i}$ is the average dislocation kinetic energy and defined as $K_{A\eta i} = \frac{1}{2} m v_{A\eta i}^2$, where *m* is the effective dislocation line mass; $b_{\eta i}$ is the Burgers vector for slip system η of the *i*-th component. L is the average distance on which the force $\tau_{\eta i} b_{\eta i}$ acts to overcome an obstacle. Since the probability of dislocations to pile-up or escape in Eq. (49) is not greater than 1, when the sign of *esc* is positive the probability is set as unity for $P_{A\eta i}^{esc}$. The resistance to dislocation motion $\tau_{\eta i}^{G}$ is defined as

$$\tau_{\eta i}^{G} = k_1 \mu b_{\eta i} \sqrt{N_{\eta i}^{I}} + \tau_0^{\eta, i}, \tag{50}$$

In which $\tau_0^{\eta,i}$ is the intrinsic lattice resistance or Peierls stress, and $N_{\eta i}^{I}$ is the dislocation impediment density defined from Cuitino and Ortiz (1993) as

$$N_{\eta i}^{I} = \left(\frac{2}{\pi}\right)^2 N^{L} + \sum_j \sum_\beta \frac{2}{\pi} \sqrt{1-\left(\mathbf{n}_{\eta i} \cdot \mathbf{n}_{\beta j}\right)^2} \left(N_{M\beta j} + N_{P\beta j}\right). \tag{51}$$

Here, N^L is the locked dislocation density. It is noted that the total change rate for a specific dislocation type $N_{A\eta i}$ during all interactions can be obtained from

$$\dot{N}_{A\eta i}^{inter} = \sum_B \sum_\beta \sum_j \dot{N}_{A\eta i - B\beta j}^{inter}. \tag{52}$$

7.2 Dislocation density evolution

For interaction between two slip systems, at least one of the two slip systems must be mobile and thus the relative velocity $\left|\boldsymbol{v}_{A\eta i - B\beta j}\right|$ in Eq. (48) is nonzero. There are three types of interactions of mobile dislocations $N_{M\eta i}$, when it meets with $N_{B\beta j}$ and cause the decreasing of the population $N_{M\eta i}$. First, mobile dislocations $N_{M\eta i}$ can pile up $\left(\dot{N}_{M\eta i - B\beta j}^{pile-M\eta i}\right)$ and become

pileup dislocations; secondly they can annihilate $\dot{N}_{M\eta i-B\beta j}^{anni-M\eta i}$ and reduce the total line density; third, they can form sessile locks $\dot{N}_{M\eta i-B\beta j}^{lock-M\eta i}$ and become sessile dislocations:

$$\dot{N}_{M\eta i}^{inter}=\sum_{B}\sum_{\beta}\sum_{j}\dot{N}_{M\eta i-B\beta j}^{inter}=\sum_{B}\sum_{\beta}\sum_{j}\dot{N}_{M\eta i-B\beta j}^{lock-Mai}+\sum_{B}\sum_{\beta}\sum_{j}\dot{N}_{M\eta i-B\beta j}^{pile-Mai}+\sum_{B}\sum_{\beta}\sum_{j}\dot{N}_{M\eta i-B\beta j}^{anni-Mai}, \quad (53)$$

in which $\dot{N}_{M\eta i}^{inter}$ is designated as the total change rate of mobile dislocation density $N_{M\eta i}$ during interactions with all other dislocations.

Based on $N_{A\eta i}=c_i\rho_{A\eta i}$, and assuming that $\dot{c}_i=0$ during plastic slip, we have

$$\dot{N}_{A\eta i}^{inter}=\dot{c}_i\rho_{A\eta i}^{inter}+c_i\dot{\rho}_{A\eta i}^{inter}=c_i\dot{\rho}_{A\eta i}^{inter}, \quad (54)$$

Further, from Eqs. (48),(53) and (54) we obtain

$$\dot{\rho}_{A\eta i}^{inter}=\sum_{B}\sum_{\beta}\sum_{j}P_{A\eta i-B\beta j}^{inter}D_{A\eta i-B\beta j}^{inter}f_{A\eta i-B\beta j}^{inter}\rho_{A\eta i}N_{B\beta j}\left|v_{A\eta i-B\beta j}\right|, \quad (55)$$

$$\dot{\rho}_{M\eta i}^{inter}=\sum_{B}\sum_{\beta}\sum_{j}\dot{\rho}_{M\eta i-B\beta j}^{lock}+\sum_{B}\sum_{\beta}\sum_{j}\dot{\rho}_{M\eta i-B\beta j}^{pile-Mai}+\sum_{B}\sum_{\beta}\sum_{j}\dot{\rho}_{M\eta i-B\beta j}^{anni-Mai}. \quad (56)$$

The dislocation density $\dot{\rho}_{M\eta i}^{inter}$ rather than $\dot{N}_{A\eta i}^{inter}$ is updated in our simulation at any local point and time. Such a treatment indicates that if a twin/ω variant with a concentration close to zero does not affect the dislocation density in other variants but $\rho_{M\eta i}$ itself of this variant ($N_{M\eta i}$ still close to zero) can be affected by other variants significantly. The advantage of updating $\rho_{M\eta i}$ rather than $N_{M\eta i}$ is that it can describe the variations of dislocation density when twinning and phase transformation occurs at different stress states. However, if the twinning or phase transformation occurs at very low stress (i.e. beginning of loading), there is no difference between updating $\rho_{M\eta i}$ or $N_{M\eta i}$. Here, it is necessary to distinguish the interactions of dislocation pileup and annihilation within the same slip system and in two different slip systems. Specifically, when the slip system $B\beta j\ (\beta j\neq\eta i)$ causes the pileup and annihilation of $M\eta i$, the pileup and annihilation occur among $M\eta i$. However, when $B\beta j=P\eta i$, there are two different interactions: first, the pileup and annihilation of $M\eta i$ take places in itself $M\eta i$ (by using symbol $\dot{\rho}_{M\eta i-P\eta i}^{pile-itself}$ and $\dot{\rho}_{M\eta i-P\eta i}^{anni-itself}$); second, pile up and annihilate occur with $P\eta i$ ($\dot{\rho}_{M\eta i-P\eta i}^{pile-MP}$ and

$\dot{\rho}_{M\eta i-P\eta i}^{anni-MP}$), which changes the dislocation density of $N_{P\eta i}$. Here $B=P$ in the sample slip system is only discussed due to $\left|\boldsymbol{v}_{M\eta i-M\eta i}\right|=0$.

Consequently, for dislocation pileup and annihilation we have

$$\begin{aligned}&\sum_{B}\sum_{\beta}\sum_{j}\dot{\rho}_{M\eta i-B\beta j}^{pile-Mai}=\sum_{B}\sum_{\beta}\sum_{j}\dot{\rho}_{M\eta i-B\beta j}^{pile-itself}+\dot{\rho}_{M\eta i-P\eta i}^{pile-MP}\\&=\sum_{B}\sum_{\beta}\sum_{j}P_{M\eta i}^{trap}D_{M\eta i-B\beta j}^{pile-itself}f_{M\eta i-B\beta j}^{pile-itself}\rho_{M\eta i}c_j\rho_{B\beta j}\left|v_{M\eta i-B\beta j}\right|+P_{M\eta i}^{trap}D_{M\eta i-P\eta i}^{pile-MP}f_{M\eta i-P\eta i}^{pile-MP}\rho_{M\eta i}c_i\rho_{P\eta i}\left|v_{M\eta i}\right|\end{aligned}\tag{57}$$

$$\begin{aligned}&\sum_{B}\sum_{\beta}\sum_{j}\dot{\rho}_{M\eta i-B\beta j}^{anni-M\alpha i}=\sum_{B}\sum_{\beta}\sum_{j}\dot{\rho}_{M\eta i-B\beta j}^{anni-itself}+\dot{\rho}_{M\eta i-P\eta i}^{anni-MP}\\&=\sum_{B}\sum_{i}\sum_{j}D_{M\eta i-B\beta j}^{anni\text{-}itself}f_{M\eta i-B\beta j}^{anni-itself}\rho_{M\eta i}c_j\rho_{B\beta j}\left|v_{M\eta i-B\beta j}\right|+D_{M\eta i-P\eta i}^{anni\text{-}MP}f_{M\eta i-P\eta i}^{anni\text{-}MP}\rho_{M\eta i}c_i\rho_{P\eta i}\left|v_{M\eta i}\right|\end{aligned}\tag{58}$$

While mobile dislocation density $N_{M\eta i}$ interacts with others causing the population reduction, there are several sources causing its increase: the homogeneous nucleation $\dot{\rho}_{M\eta i}^{gen}$, the mobile dislocation propagation from a set of dislocation sources $\dot{\rho}_{M\eta i}^{prop}$, and the escape of pileup dislocations $\dot{\rho}_{P\eta i}^{esc}$. The total mobile dislocation density in the slip system η of the *i*-th phase yields:

$$\dot{\rho}_{M\eta i}=\dot{\rho}_{M\eta i}^{gen}+\dot{\rho}_{M\eta i}^{prop}+\dot{\rho}_{P\eta i}^{esc}-\dot{\rho}_{M\eta i}^{inter}.\tag{59}$$

The homogeneous nucleation of dislocations $\dot{\rho}_{M\eta i}^{gen}$ occurs within a perfect lattice, which requires large thermal fluctuations or external stress. It is only considered in the theoretical development in Eq. (59) but is ignored in our simulation, as Hansen, *et al*. (2013), Luscher *et al*. (2017). The mobile dislocation propagation $\dot{\rho}_{M\eta i}^{prop}$ is defined as

$$\dot{\rho}_{M\eta i}^{prop}=k_{\eta i}\rho_{M\eta i}\left|v_{\eta i}\right|/\overline{r}_{M\eta i},\tag{60}$$

Here, the material parameter $k_{\eta i}$ is the propagation coefficient and $\overline{r}_{M\eta i}$ is the average mobile dislocation loop radius of curvature.

Two sources can cause the escape of pileup dislocations $\dot{\rho}_{P\eta i}^{esc}$. One is the thermal escape of pileup dislocations $\dot{\rho}_{P\eta i}^{esc\theta}$ during the thermal fluctuation with assistance of external forces:

$$\dot{\rho}_{P\eta i}^{esc\theta} = \frac{1}{t_{P\eta i}^{esc\theta}} P_{P\eta i}^{esc}, \tag{61}$$

where $t_{P\eta i}^{esc\theta}$ is the time constant equal to the average time of a thermal fluctuation, which is the mean phonon frequency; $P_{P\eta i}^{esc}$ is defined in Eq. (61). The other source $\sum_{\beta}\sum_{j}\dot{\rho}_{P\eta i-M\beta j}^{esc-inter}$ is caused by pileup dislocation escape by interacting with the mobile dislocations of each slip system based on Eq. (55).

Pileup dislocations are generated due to the pileup of mobile dislocations on obstacles, and its population reduces due to the escape, annihilation, and lock formation. The evolution of pileup dislocations is given as below:

$$\dot{\rho}_{P\eta i} = \sum_{B}\sum_{\beta}\sum_{j}\dot{\rho}_{M\eta i-B\beta j}^{pile-Mai} - \dot{\rho}_{P\eta i}^{escT} - \sum_{\beta}\sum_{j}\dot{\rho}_{P\eta i-M\beta j}^{esc-inter} - \dot{\rho}_{M\eta i-P\eta i}^{anni-MP} - \sum_{\beta}\sum_{j}\dot{\rho}_{P\eta i-M\beta j}^{lock-inter}. \tag{62}$$

While locked sessile dislocations do not belong to any slip system, they do affect mobile dislocation motion and also affect the pileup dislocation escape, as shown in Eqs. (51) and (61). The locked dislocation density is generated as mobile dislocations interact with pileup or mobile dislocations to leave sessile locked debris in the materials

$$\dot{N}^{L} = \sum_{M\eta i}\sum_{B\beta j} N_{M\alpha i-B\beta j}^{lock} = \sum_{M\eta i}\sum_{B\beta j} P_{M\eta i-B\beta j}^{lock} D_{M\eta i-B\beta j}^{lock} f_{M\eta i-B\beta j}^{lock} N_{M\eta i} N_{B\beta j} \left|\boldsymbol{v}_{A\eta i-B\beta j}\right|. \tag{63}$$

Here, $f_{M\eta i-B\beta j}^{lock}$ is the fraction of collisions that form locks. The probability $P_{M\eta i-B\beta j}^{lock} = 1$ was used in (Hansen *et al*., 2013) because the energy releases during the formation of locks.

7.3 Dislocation evolution during twinning and phase transformation

One of the questions in this area is how the dislocation density varies during phase changes or twinning. In some case such as from the α to ω phase, or from the ω to β phase in Ti, the total number of slip systems and the types of slip systems can change. Therefore, the dislocation density in one slip system in one phase will not be preserved into another during phase transformation. For example, some mobile/immobile dislocations may become immobile/mobile after a phase change. Some possible mechanisms for this interaction can be found in the work of Levitas and Javanbakht (2015) and Javanbakht and Levitas (2015), where the inheritance of state variable quantities of plastic slip during phase transformations are proposed.

It remains an open question that for cases of material volumes transforming through twinning or structural processes, how the existing dislocation state is effected by that transformation. Given the complexity of dislocation structure in a deformed material there are many ways in which the pattern of stacking faults which include mobile and immobile portions could possibly change through a crystallographic transformation process. This mapping may also be influence by the atomic structure similarity between phase 1 and phase 2. It is difficult to imagine that a direct mapping of dislocation structure between two very different crystallographic structures would take place without significant change. Given that we are interested in the transformation from an HCP system to an HEX system, where both systems are fundamentally similar, we will take the conservative step to assume that when the material component *i* transforms to the component *j* by twinning or phase transformation, the newly transformed component *j* has the same dislocation density $\rho_{A\eta i}$ with the existing variant *j*. Assuming that we know the initial dislocation density $\rho_{A\eta i}$ in all slip systems for both phases before loading is applied, we can update $\rho_{A\eta i}$ during loading by Eq. (55) even though the volume fraction c_i is zero and thus we can obtain the dislocation density when twinning and phase transformation occur. When the phase transformation or twinning occurs, the total dislocation location density $N_{A\eta i}$ for this new phase or new twin having a volume fraction c_i : $N_{A\eta i} = c_i \rho_{A\eta i}$.

8. Evolution of temperature

The temperature can be updated by the total dissipation energy converted into thermal energy and stored in the material. Therefore, the temperature variation based on the second law of thermodynamics follows:

$$\dot{\theta} = \frac{1}{\rho c_v}\left(k_1 \sum_i \sum_\beta c_i \tau_{\beta i} \dot{\gamma}_{sl-\beta i} + k_2 \sum_j \tau_{j-tw} \gamma_{tw} \dot{c}_{j-tw} + k_3 \sum_m X_{m-pt} \dot{c}_{m-pt} \right), \tag{64}$$

where the specific heat at constant volume $c_v = -q\frac{\partial^2 y}{\partial q^2}$; k_1 , k_2 and k_3 are the ratios of dissipative energy during plastic slip, twinning, and phase transformation respectively stored as the thermal energy in the material. Here we take 0.8 as the magnitude for each of these three ratios. For the experiment in Morrow *et al*. (2017a), the time for shockwave transmission from the impact plane to free surface plane is less than 0.5 μs . Therefore, we assume adiabatic

conditions. More detail on the non-equilibrium thermodynamics of dislocation slip processes can be found in Lieou and Bronkhorst (2018) and Lieou *et al*. (2018).

9. Experiment, model, and material parameters for plate impact experiment

9.1. *Multi-crystal experiment*

Plate impact experiments under uniaxial strain loading have long been valuable for investigating the deformation characteristics of materials at high strain rates (e.g. Winey and Gupta, 2004, 2006; Becker, 2004, Barton *et al*., 2005). Plate impact experiments were conducted on a high-purity Ti multi-crystal sample composed of four large grains as presented in Morrow *et al*. (2017a), with each grain extending completely through the specimen thickness. Each grain represented a different crystal orientation relative to the impact load direction. The loading direction was along $[0001]$, $[10\bar{1}1]$, $[10\bar{1}0]$, and $[3\bar{1}\bar{4}4]$ orientations of these four crystals (See Fig. 2). The thickness of the polycrystalline copper flyer and the titanium sample were 2.032 mm and 1.502 mm, respectively. The diameter of the flyer was 38 mm. The 10.06 mm diameter Ti sample was embedded in a standard polycrystalline Ti momentum trap ring assembly. The velocity of the projectile was measured as 0.956 mm/μs before impact. A peak pressure in the Ti sample was estimated as 14.5 GPa and the pressure of phase transformation was estimated as 13.5 GPa for the [0001] crystal. A photon Doppler velocimetry (PDV) probe was targeted onto each of the crystals to measure the free surface velocity, opposite the impact surface. A similarly deformed bi-crystal of [0001] and $[10\bar{1}1]$ orientations were also soft-recovered for post-test examination. In this paper, to discover the possible physics happening in the crystals under high strain rate, two shocked crystals of $[0001]$ and $[10\bar{1}1]$ orientation were sectioned to examine the components of material by EBSD. The dimensions of the sample are such that any wave interactions due to grain boundaries will not influence the free-surface velocity traces. There is a greater possibility of an influence of the grain boundaries on the recovered sample structure, but this is expected to be minor and the metallography was performed near the grain center so as to minimize any residual effects. The volume fractions of the α parent material, primary and secondary twins of the α phase, and the ω variants are reported in this paper and will be discussed in detail in the next section.

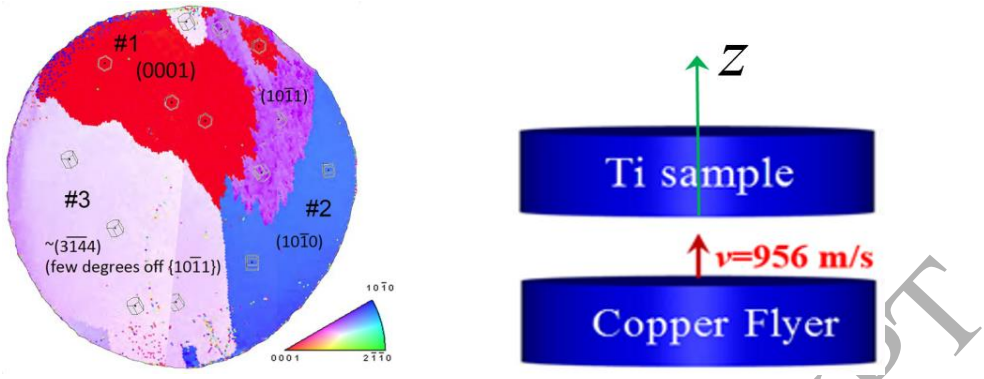

(a) (b)

Fig. 2. Micrograph of the Ti multi-crystal sample (a), adopted from (Morrow *et al*., 2017a). A simple schematic of plate impact experiment (b) which is not to scale. In (b), the *z* axis is along the thickness of sample and at the impact plane *z*=0. The sample diameter is 10.06 mm embedded in a momentum trapping ring assembly, and the sample thickness is 1.502 mm.

9.2. Modeling of plate impact experiments

The finite element code ABAQUS/explicit is used for the uniaxial strain simulation of $[0001]$ and $[10\bar{1}1]$ direction uniaxial strain loading plate impact experiments. The system of constitutive equations are coded into a VUMAT subroutine by fully explicit time integration. Three hundred elements are assigned along the thickness of the sample, and one element in the direction perpendicular to the impact loading, which significantly reduces the computation time in comparison with three-dimensional geometry. Our results are not time-step size and mesh size dependent. Specifically, we divided the total loading time into 10,000 and 20,000 equal-time steps, and assigned 300 and 600 elements in the thickness direction with the element type as an 8-noded brick element (C3D8). For all of these cases, we obtained the same simulation results. In addition, the loading direction is along the *z* axis as shown in Fig. 2b, and one element assigned in the direction perpendicular to the *z* axis is also reasonable since the obtained results will show that the anisotropy in the *x* and *y* directions is negligible. It was also proven for single crystal Ti under SPHB in Feng *et al*. (2018a), where the anisotropy in the lateral directions are negligible using a three-dimensional model. In this paper, we only consider the compressive portion of shock loading and not the later time release, and thus the possible reverse phase transformation or detwinning during the unloading process are not considered. The copper flyer is represented

by applying the velocity 600 m/s at the impact plane during the compression. Such a one-dimensional FEM model is also widely utilized for modeling the plate impact experiment (see examples in (Luscher *et al*., 2017; Addessio *et al*., 2017)).

9.3 Material parameters for twinning, slip, and phase transformation

HCP metals such as Mg, Ti, and Zr, generally display pyramidal $\langle a+c \rangle$, prismatic $\langle a \rangle$, and basal slip modes. For Ti, pyramidal $\langle a+c \rangle$ and prismatic $\langle a \rangle$ slips are the active modes (Yoo *et al*., 2001; Clouet *et al*., 2015; Nervo *et al*., 2016; Morrow *et al*., 2016; Feng *et al*., 2018a). Based on symmetry, there are 12 pyramidal slip systems and 3 prismatic slip systems for the α phase. For the ω phase of Ti, there are 3 prismatic and 3 basal slip systems. Six tensile $\{10\bar{1}2\}\langle\bar{1}011\rangle$ and six compressive $\{11\bar{2}2\}\langle 11\bar{2}\bar{3}\rangle$ twinning modes are commonly observed to be active for simple compression deformation in Zr and Ti single crystals (Beyerlein and Tomé, 2008; Morrow *et al*., 2016, 2017a). From the experiments (Morrow *et al*., 2016, 2017a) and the pole figures from this paper, compressive twinning is the primary twinning mode and tensile twinning is the secondary twinning mode. In our plate impact simulations, we consider the secondary twinning process, which is treated in the same way as in Feng *et al*. (2018a). The volume fraction of the secondary twins is small and they are located in very thin layers. Consequently, for simplicity, we ignore slip and phase transformation in the secondary twins, which is consistent with experimental observations. Plastic slip is considered in all components of parent material, primary twins, and ω components, but for simplicity is not allowed within secondary twins.

The Burgers vector magnitude in the prismatic and pyramidal slip systems of the α phase are 0.29 nm and 0.55 nm, respectively (Yoo *et al*., 2001). Gong *et al*. (2015) found that there is a greater resistance to motion for dislocations with a larger Burger's vector, and thus salient differences in the intrinsic lattice resistance $\tau_0^{\alpha,i}$. Values for α phase pyramidal $\left(\tau_0^{\alpha,i} = 800\,\text{MPa}\right)$ and prismatic $\left(\tau_0^{\alpha,i} = 37\,\text{MPa}\right)$ slip systems are used in Eq. (50) (Beyerlein and Tomé, 2008). Similarly, for the ω phase, the Burger's vector magnitude and $\tau_0^{\alpha,i}$ for the basal slip are 0.47 nm and $900\,\text{MPa}$, respectively, and for prismatic slip modes they are 0.29 nm and 90MPa in this paper (Beyerlein and Tomé, 2008). Except for Burger's vectors and $\tau_0^{\alpha,i}$, all other

material parameters are the same for all slip systems in $[0001]$ and $[10\bar{1}1]$ crystals between both α and ω phases. The parameter magnitudes are the same as what was reported by Feng *et al*. (2018a) for the $[0001]$ crystal loading orientation. An exception being the initial mobile dislocation density for all slip systems $\rho_{M\beta i}\big|_{t=0} = 3.0\times10^{12}$ employed here. It is also noted that in Eq. (46), the drag coefficient $B_{\beta i} = B_0 \Big/ \left[1-\left(v_{\beta i}/c_s\right)^2\right]$ is not considered in Feng *et al*. (2018a) due to non-shock loading and small $v_{\beta i}$. The shear sound speed c_s, for Ti is 3210 m/s, and longitudinal sound speed c_l is 6100 m/s. For plate impact loading, a resolved shear stress threshold of 1.2 GPa is used for the dislocation velocity expression in Eq. (46) so that for a value below this magnitude, mobile dislocation velocity is zero.

For phase transformation, the material parameters in Eq. (43) are given in Table 4. For simplicity, hardening for twinning in Eq. (41) is ignored, and the parameters for twinning in Eq. (40) are listed in Table 5. For $[0001]$ and $[10\bar{1}1]$ orientation loaded crystals, we only use one parameter, τ_{tw0}, with different values for each simulation. All other material parameters for elasticity, plastic slip, twinning, and phase transformation are consistent for both experiments. τ_{tw0} is the material parameter that the shear stress must overcome to initiate twinning, which is an increasing function of TSFs. TSFs is some quantification of the degree of disorder in materials, which can be generated during plastic slip (Levitas *et al*., 2006) and for the $[0001]$ crystal having larger plastic slip deformation than that in the $[10\bar{1}1]$ crystal, as it will be shown in Section 10. Therefore, we use a higher τ_{tw0} in the $[0001]$ crystal. In addition, for phase transformation and twinning, if the component *i* changes into the component *j*, we assume that such change occurs only when the volume fraction of the component *i* is above 0.005.

Quantity (Unit)	p_1 (1)	w (1/s)	β_{tr} (J/m^3)	q_1 (1)	ε_{v-pt} (1)
Magnitude	2.0	13.0×10^6	30.0×10^7	2.0	0.017

Table 4. Values of material parameters used to represent the process of phase transformation found in Eq. (43).

Quantity (Unit)	b_0 (1)	γ_{tw} (1)	S_{tw0} (GPa)	$\dot{\gamma}_0$ (1/s)	τ_{tw0} (GPa) for [0001] crystal	τ_{tw0} (GPa) for $[10\bar{1}1]$ crystal	d_0 (1)
Magnitude	2.0	0.216 (primary) /0.177 (secondary)	15 (primary) /30(secondary)	40.0e4	1.0 (primary) /1.6 (secondary).	0.2 (primary) / 0.8 (secondary).	0.6

Table 5. Single crystal HCP Ti material parameters for twinning. When there is no indication of primary or secondary twinning, it means the value for both primary and secondary twinning processes in Eq. (40).

10. Discussion of Results

In this section, the results of [0001] and $[10\bar{1}1]$ direction plate impact experiment simulations are discussed.

10.1 The [0001] crystal direction loading

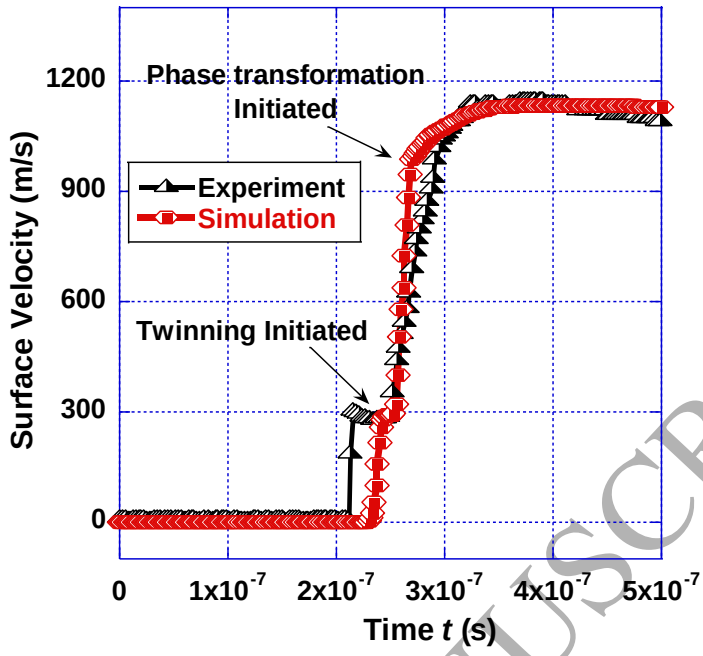

Fig. 3. The free surface velocity from experiment (Morrow *et al.*, 2017a) and simulation for the $[0001]$ crystal orientation loading.

The free surface velocity results for both simulation and experiment is plotted in Fig. 3 for the $[0001]$ crystal orientation loading. The results demonstrate that a reasonably good correspondence between simulation and experiment is obtained. When the free surface velocity reaches 300 m/s, twinning initiates, and a plateau in velocity is found in both experiment and simulation. After this plateau, the slope is slightly smaller than the elastic front because the dissipative twinning and slip occur during the time when the free surface velocity is between 300 to 1000 m/s. Phase transformation appears at a free surface velocity of approximately 1000 m/s, which causes a reduction of slope in the free surface velocity curve. At later times, the free surface velocity becomes stable with a magnitude around 1100 m/s in both simulation and experiment. The evolution of material state through the thickness of the sample is given in Figs. 4c and 4d. The internal sample particle velocity curve versus sample thickness (the *z*-axis) has the same features as free surface velocity versus time. From Fig. 4c, the relative particle velocity $\left(\frac{v}{600(\mathrm{m/s})}\right)$ reaches 0.25, and there is a plateau in the curve, while the volume fraction of the

primary twins is almost zero. However, the resolved shear stress has just reached the critical value $\tau_{tw0} = 1.0$ GPa in this region and thus the primary twinning can take place in spite of the small volume fraction. Consequently, this initiation of twinning causes both plateaus in the particle velocity curve and resolved shear stress curve, as shown in Fig. 4c. With an increase of resolved shear stress after this plateau region, the volume fraction of primary twins increases very fast as shown in Fig. 4c. When the resolved shear stress reaches maximum, the primary twin volume fraction has not reached maximum until the relative resolved stress $\left(\frac{\tau_{tw\text{-}1}}{1.0\,\text{GPa}}\right)$ has been reduced to the value of about 1.0. At the maximum twin volume fraction, phase transformation initiates as shown in Fig. 4d. With phase transformation, the volume fraction of primary twins gradually decreases and the ω phase volume fraction increases. In addition, the phase transformation leads to a drop of the absolute value of slope in the particle velocity of the sample in Fig. 4d. Fig. 4b shows the volume fractions of parent material (c_0), each primary twin ($c_1 - c_6$) and the ω component ($c_8 - c_{13}$) at time $t = 0.145\,\mu$s. In this paper, and as described earlier, numbers 0-13 are used for the components of materials and their orientations and these numbers are used to help in explaining the pole figure results. Secondary twinning is found in only small quantities and occurs only at the region close to the impact plane as shown in Fig. 4a. This is attributed to boundary effects. During compression, in most of the sample, we did not find secondary twins, which is also consistent with experimental results shown in Fig. 5 and Table 6. It is noted that the total volume fraction of primary material, the six primary twins and six omega components marked by circles in Figs. 5a and 5b is 95.6% as listed in Table 6. The intersection angles between the shock wave direction (i.e. the *z*-axis) and the twinning plane or twinning direction are the same for all six primary twin variants in the [0001] crystal. As a result, the volume fractions for each primary twin variant are the same as shown in Fig. 4b. The driving force in Eq. (42) for phase transformation from each primary twin are the same as well due to equal primary twin volume fraction. Thus, we obtain an equal amount for the six ω components in Fig. 4b, which is consistent with experimental results as shown in Fig. 5b and Table 6. Behind the shock wave, the parent material phase remains the majority fraction as shown in Fig. 4b, which is also consistent with experimental results presented in Fig. 5a and Table 6.

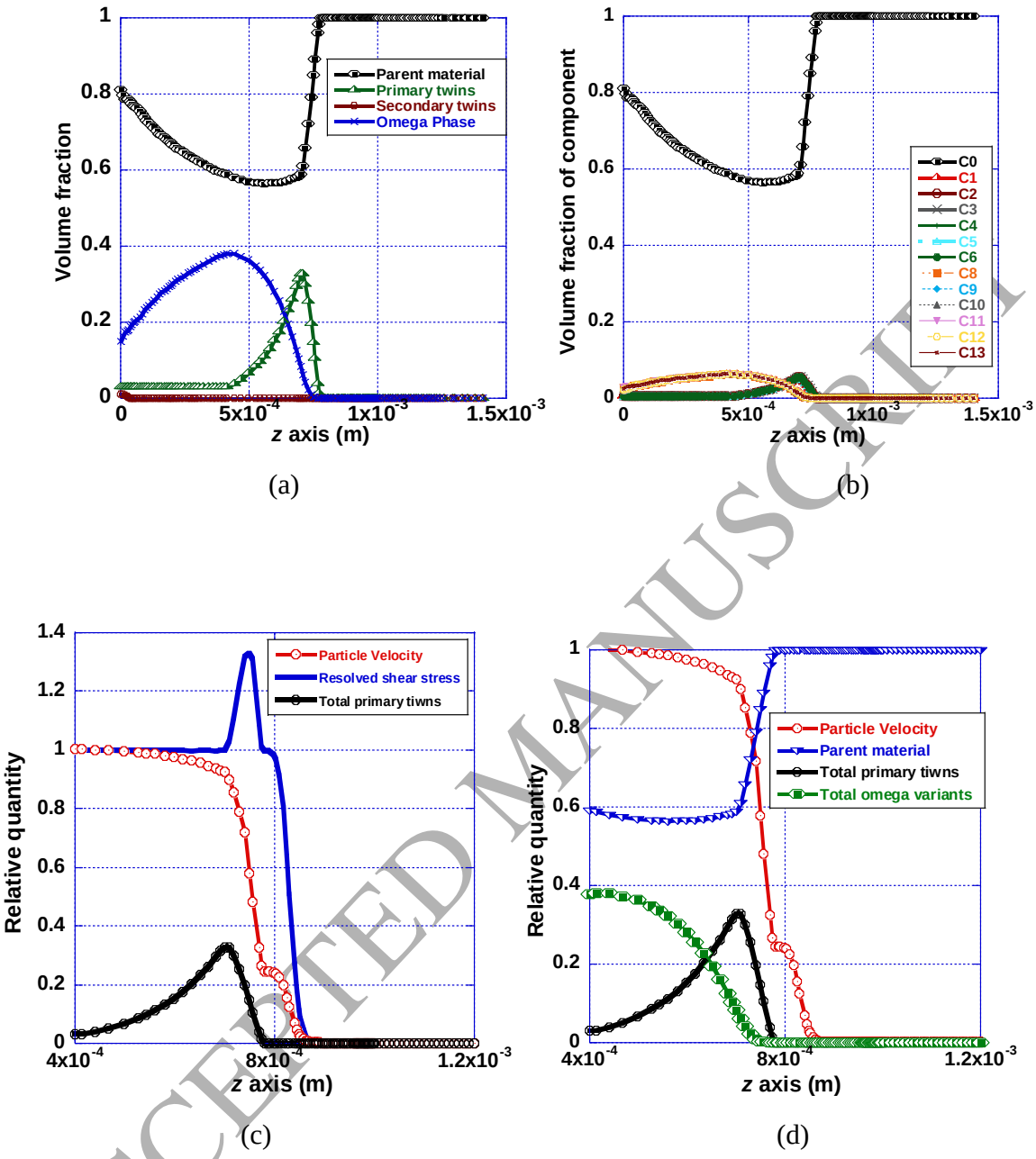

Fig. 4. (a) Distribution in volume fractions of the parent material, total primary twins, total secondary twins, and total ω components. (b) the volume fractions of parent material (c_0), each primary twin ($C_1 - C_6$) and the ω component ($C_8 - C_{13}$), and their orientation are marked in Fig. 5. (c) The relative particle velocity $\left(\frac{v}{600(\mathrm{m/s})}\right)$, the volume fractions of total primary twins, and

the relative resolved shear stress $\left(\frac{\tau_{tw\text{-}1}}{1.0\,\text{GPa}}\right)$ for the primary twin c_1. (d) The relative particle velocity, the volume fractions of the parent material, total primary twins, total secondary twins, and total ω components. All figures are along the thickness direction (the z-axis) and the time instant is $t = 0.145\,\mu\text{s}$ for the $[0001]$ crystal direction loading.

Pole figures from EBSD performed on the sectioned recovered samples provide very important information for the volume fractions of material components and crystal orientations. Recall however, the recovered samples have experienced release which our theory and simulations do not yet account for. In this paper, we take the recovered sample from (Morrow *et al.*, 2017a) and obtain the pole figure in Figs. 5 and 12, and the volume fractions for material components in Tables 6 and 7 for both $[0001]$ and $[10\bar{1}1]$ crystal orientation samples. Fig. 5c from the simulation rotation tensors shows that the locations of the twinned α components and corresponding ω components are the same and there is a large rotation between the ω components and the parent material as discussed earlier. Figs. 5a and 5b show that there is no large lattice rotation during phase transformation as well, while all poles of ω component radially move slightly to the center. Since the lattice axes a_1 and a_2 among six primary twins are not symmetric to the loading direction (the z-axis), there is no rotation tensor in transformation deformation $\mathbf{F}_t$ which can lead to these slight radial movements. Fig. 5c shows the rotation angles during twinning and phase transformation, which are consistent with the experimental pole figures for all alpha components and slight difference in the omega components. The difference in pole figures for the ω phase between simulation and experiment in Fig. 5 may exist for two reasons. First, the simulation pole figure of the ω phase only corresponds to the rotation angle during twinning $\mathbf{F}_{tw}$, while the experimental one is the c axis of the ω phase in the recovered sample after unloading potentially affected by twinning, slip, and elastic processes. The concentration of ω phase is not large and has the characteristic lenticular shape due to elastic interaction between the omega and alpha phases. Implied in this is that the hypothesized pathway for phase transformation was through the primary twin fraction in the material. It may be that this hypothesis may not be entirely correct. Secondly, even though $\mathbf{F}_e = \mathbf{R}_e \cdot \mathbf{U}_e$ can be

released into a unit tensor, $\mathbf{F}_{sl}$ may not be a symmetric tensor, which affects the magnitude of $\mathbf{R}_e$ (i.e. the unloading route) and thus causes the rotation of the *c* axis. It must also be stated again that the sample has experienced the release portion of loading, whereas this was not possible with the present model. Therefore one must consider that some additional slip and twinning activity may have taken place and proportion of phase reversion back to α cannot be ruled out.

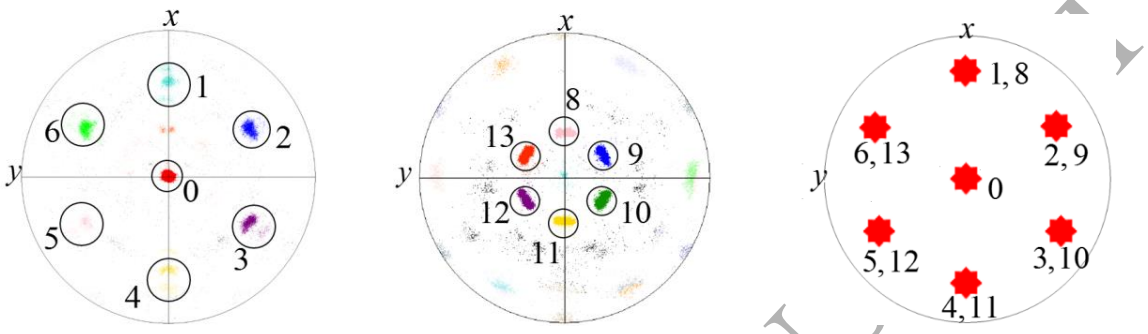

(a) (b) (c)

Fig. 5. Pole figures from experiment (a, b) and simulation (c). (a) is for the α phase and (b) is for the ω phase from experimental EBSD measurements. The total volume fraction for the marked circle region in (a, b) is equal to 95.6% as list in Table 6, and thus there are some poles in (a, b) unmarked which is negligible due to a low fraction. (c) is the pole figure for the rotation tensor **R** during twinning and phase transformation from the initial parent material. Number 0 is for parent material, 1-6 stand for the α primary twins and 8-13 for the ω phase, which are listed in Table 1.

Component	Volume fraction in experiment	Volume fraction in simulation
0	0.669	0.590
1	0.004	0.005
2	0.008	0.005
3	0.008	0.005
4	0.002	0.005
5	0.001	0.005
6	0.006	0.005
8	0.034	0.064
9	0.043	0.063
10	0.054	0.063
11	0.032	0.064
12	0.054	0.063
13	0.041	0.063

Total above	0.956	1.0

Table 6. Volume fraction of components in both experiment and simulation for the [0001] crystal orientation loading. Component number 0 is the parent material, 1-6 stands for the primary twins, 8-13 represent the ω components. Simulation is from a representative location ($z = 5.0\times10^{-4}\,\mathrm{m}$ at $t = 0.145\,\mu\mathrm{s}$), when the volume fractions become stable (i.e. unchanged) during the compressive shock wave. Such location and time instant are also used for Table 7.

Table 6 presents the volume fractions of the parent material, the primary twins, and the ω components from both simulation and experimental results. Reasonably good correspondence between simulation and experiment in volume fractions of components is obtained. It is found that the α parent material is the dominant component, which is different from the SHPB results presented in Feng *et al.* (2018a). In the SHPB experiment (Feng *et al*., 2018a), the parent material is twinned almost completely while the stresses are much smaller. The volume fraction of the ω phase components are the second highest in magnitude, with a similar volume fraction among each of the six components. The volume fraction of the primary twins is next in magnitude order and much less than the parent material and the ω phase components.

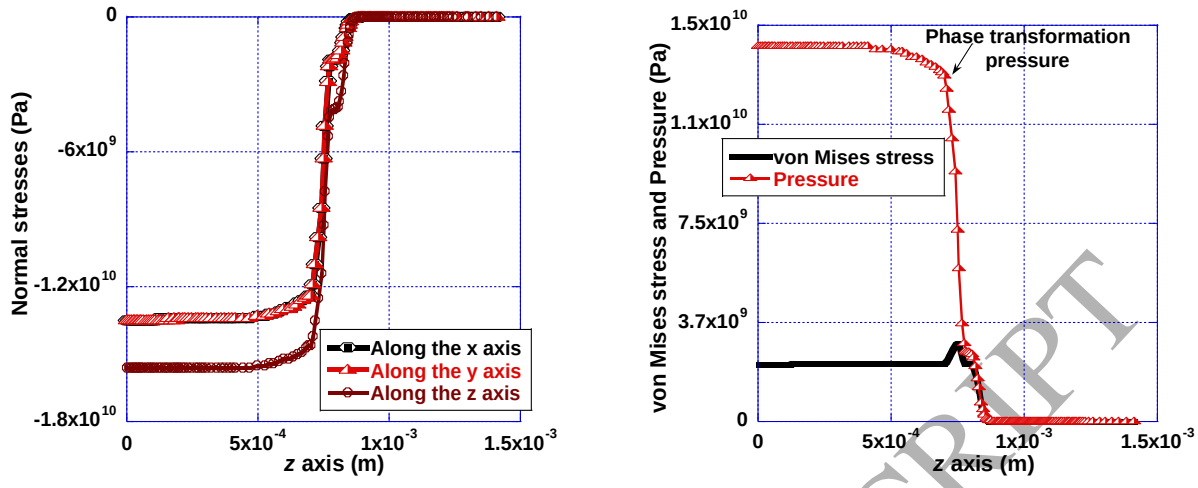

(a) (b)

Fig. 6. (a) Normal stresses $\left(\sigma_{xx}, \sigma_{yy}, \text{and } \sigma_{zz}\right)$, and (b) pressure and von Mises stress versus distance through the sample thickness for the [0001] crystal orientation loading.

For plate impact experiment under the conditions of the predominantly one-dimensional strain loading, the normal stresses $\left(\sigma_{xx}, \sigma_{yy}, \text{and } \sigma_{zz}\right)$ are nonzero but all of shear stresses $\left(\sigma_{xy}, \sigma_{zy}, \text{and } \sigma_{xz}\right)$ are zero, while for SHPB the only nonzero stress is σ_{zz} but the strains are three dimensional. Fig. 6a shows that the magnitude of the normal stress $\left|\sigma_{zz}\right|$ is around 12% greater than the lateral stress $\left|\sigma_{xx}\right|$ and $\left|\sigma_{yy}\right|$, and $\left|\sigma_{xx}\right|$ and $\left|\sigma_{yy}\right|$ are the same due to coexistence of many components with different orientations and small anisotropy in elasticity for HCP Ti (Feng *et al*., 2018a). It also suggests that the one-dimensional model for plate impact experiment is suitable. The maximum shear stress is equal to $\frac{\sigma_{xx}-\sigma_{zz}}{2}$ and is much smaller than any of the normal stresses. Similarly, Fig. 6b shows that the von Mises stress is much smaller than the pressure. In addition, the peak pressure in Fig. 6b is 14.2 GPa, which is consistent with the experimental value of 14.9 ± 0.2 GPa found in Morrow *et al*. (2017a). The phase transformation occurs at a pressure above 13.0 GPa, which is also consistent with estimated experimental transition pressure of 13.5 GPa arrived at in Morrow *et al*. (2017a). Such a high transformation pressure under high-strain-rate loading is much larger than the reported pressures from static loadings in literature (Jayaraman *et al*., 1963; Sargent and Conrad, 1971; Vohra, 1978; Sikka *et*

al., 1982; Singh *et al*., 1982; Xia *et al*., 1990; Razorenov *et al*., 1995; Akahama *et al*., 2001, 2002; Vohra and Spencer, (2001); Cerreta *et al*., 2006a,b; Saxena *et al*., 2015; Morrow *et al*., 2017a). Consequently, phase transformation is a strain rate dependent process and high strain rate can impede the rate of transformation kinetics.

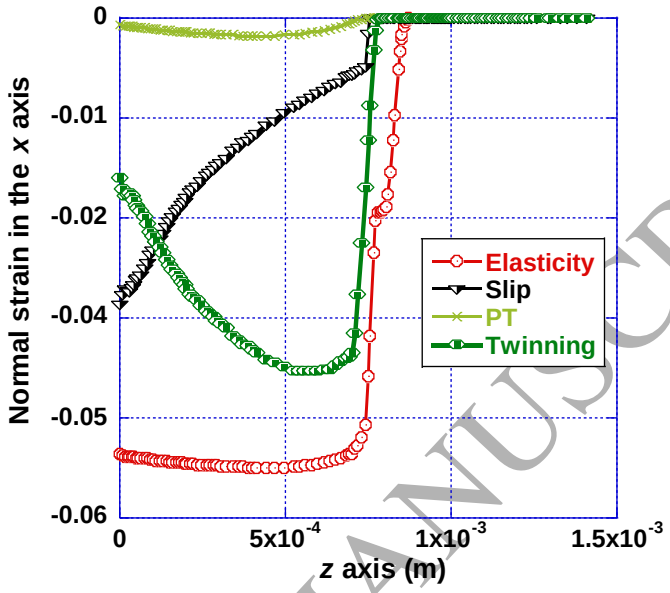

Fig. 7. The axis normal strains due to elasticity $(\varepsilon_{zz\text{-}e})$, slip $(\varepsilon_{zz\text{-}sl})$, twinning $(\varepsilon_{zz\text{-}tw})$, and phase transformation $(\varepsilon_{zz\text{-}pt})$ versus the *z* coordinate for the [0001] crystal at $t = 0.20\,\mu s$.

Since we are assuming a strictly uniaxial strain loading, the only nonzero strain component is the normal strain ε_{zz}. Fig. 7 plots the axial direction normal strains due to elasticity, slip, twinning, and phase transformation. Their definitions are the logarithmic strains for the axial components of deformation gradients $\mathbf{F}_e, \mathbf{F}_{tw}, \mathbf{F}_{pt}$ and $\mathbf{F}_{sl}$. For example, the axial elastic normal strain is $\varepsilon_{zz\text{-}e} = \ln F_{e33}$ and the axial phase transformation normal strain is $\varepsilon_{zz\text{-}pt} = \ln F_{pt33}$. The largest contribution to the axial compressive deformation is elastic, which is mostly caused by elastic volumetric contraction due to high pressure. Twinning deformation is smaller than the elastic deformation, and both are much larger than the axial deformation caused by phase transformation and plastic slip, except for the region close to the impact plane where the deformation of plastic slip can surpass the twining deformation. The transformational volumetric strain is -0.017 from α to ω phase transformation. In the extreme case with a complete phase

transformation, the maximum axial normal strain is only -0.017/3=-0.0057, while the sum of two lateral normal strains are -0.017/3*2=-0.0113. Consequently, the axial deformation due to phase transformation cannot be large as shown in Fig. 7. While the dislocation density is not small, and such a magnitude can cause large deformation in SPHB, where strain magnitudes are much greater. However, plastic slip deformation is small in Fig. 7, in comparison with deformation due to twinning or elasticity, while close to the impact plane it is slightly larger than twinning deformation due to longer deformation time than the time at the region close to the elastic front. Fig. 8 shows that for an initial temperature of 298 K, the maximum temperature is 380 K at the region close to the impact plane which is a little higher than other regions. This is because the temperature growth due to plastic slip decreases from the impact plane to the elastic front. While the twinning deformation is much larger than that due to phase transformation as shown in Fig. 7, the temperature increase due to twinning is only slightly higher than the effect from phase transformation. This is because the pressure is over 10 times higher than the resolved shear stress as we can see in Figs. 4c and 6b, which increases the dissipative energy for phase transformation.

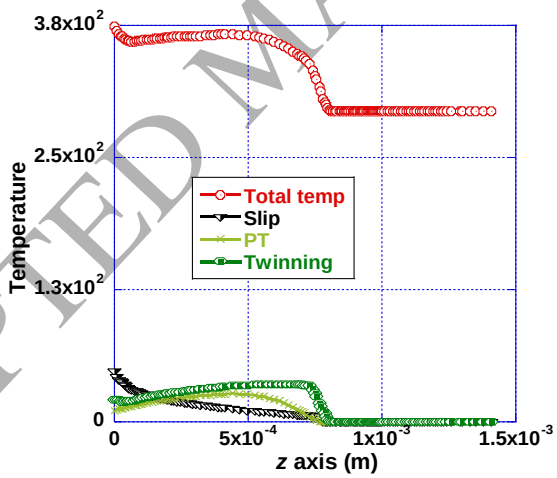

Fig. 8. The temperature within the sample, and temperature variations due to slip, phase transformation, and twinning for the [0001] crystal at $t = 0.145\mu s$.

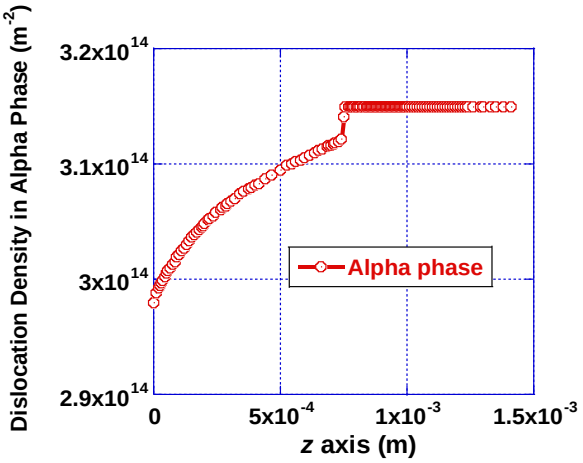

(a)

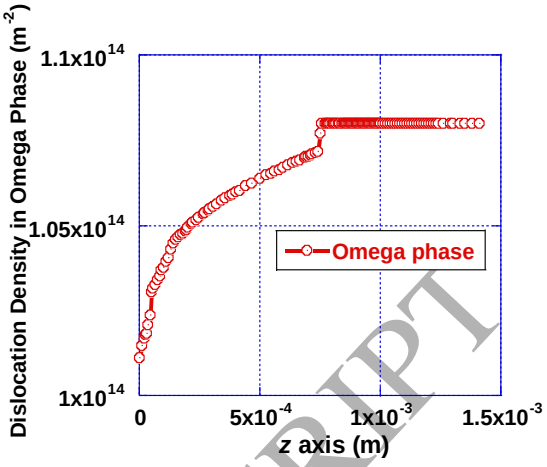

(b)

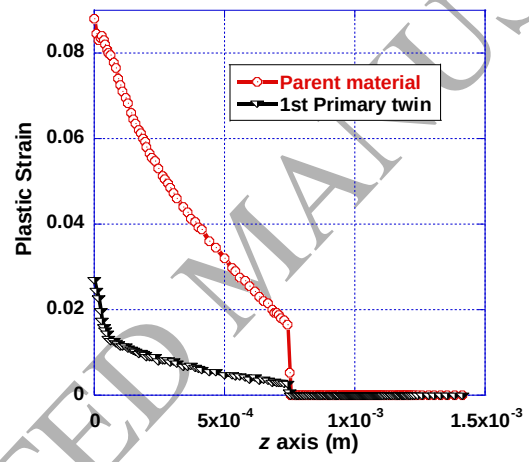

(c)

Fig. 9. The total dislocation density in the α (a) and ω (c) phases, and (c) plastic strain in the parent material and primary twin variant number 1. Only variant 1 is shown since the other variants show similar magnitude evolution due to sample symmetry. Here, the total dislocation density is the summarization of all slip systems of the α or ω phase without being multiplied by their volume fraction of phases: $\sum_{\eta,i} \rho_{M\eta i} + \rho_{P\eta i}$.

During very short shockwave transmitting time as observed in this work, the variation of dislocation density is very small as shown in Figs. 9a and 9b. The number of slip systems is 15 for the α phase and 6 for the ω phase. During phase transformation, the total dislocation density

of the material (the sum of both phases) decreases since the number of slip systems for the ω phase is only 6. Figs. 9a and 9b plot the dislocation density in all slip systems of the α and ω phases along the sample thickness. During the impact, the dislocation density slightly decreases for both phases because the multiplication of dislocation is slower than the annihilation of dislocation. Fig. 9c plots the plastic strain deformation from Eq. (45), which is defined by

$$\gamma_{i-sl} = \int_0^t \sum_\beta \dot{\gamma}_{\beta i}\,\mathrm{d}t = \int_0^t \sum_\beta b_{\beta i}\rho_{M\beta i}v_{\beta i}\mathrm{d}t\ . \tag{65}$$

Here i=0 for parent material, and i=1 for the primary twin number 1. Since the volume fraction of the i-th component is not in the integration of Eq. (65), the plastic strain is the value inside of the i-th component instead of in a representative volume of material. Fig. 9c shows that the plastic strain is larger in the parent material than that in the primary twins, even though we ignore the plastic strain hardening caused by the twinned material localized in thin layers. It is known that the plastic deformation can increase the degree of disorder (i.e. TSFs) that causes a large barrier for phase transformation (Levitas *et al*., 2016). In this paper, for this reason and also consistent with experimental and previous computational results, we did not consider the phase transformation in the parent material but only in the primary twins.

10.2 The $[10\bar{1}1]$ *crystal direction loading*

The free surface velocity is plotted for both simulation and experiment in Fig. 10a. While we were not able to obtain it for the $[10\bar{1}1]$ crystal, the free surface velocity for the $[3\bar{1}\bar{4}4]$ crystal is available and its orientation is only a few degrees orientation difference from the $[10\bar{1}1]$ crystal. The free surface velocity from both simulation and experiment in Fig. 10a shows that at a velocity around 900 m/s there is a significant drop in the slope, which is caused by the twinning and slip processes, and the final velocity is around 1160 m/s.

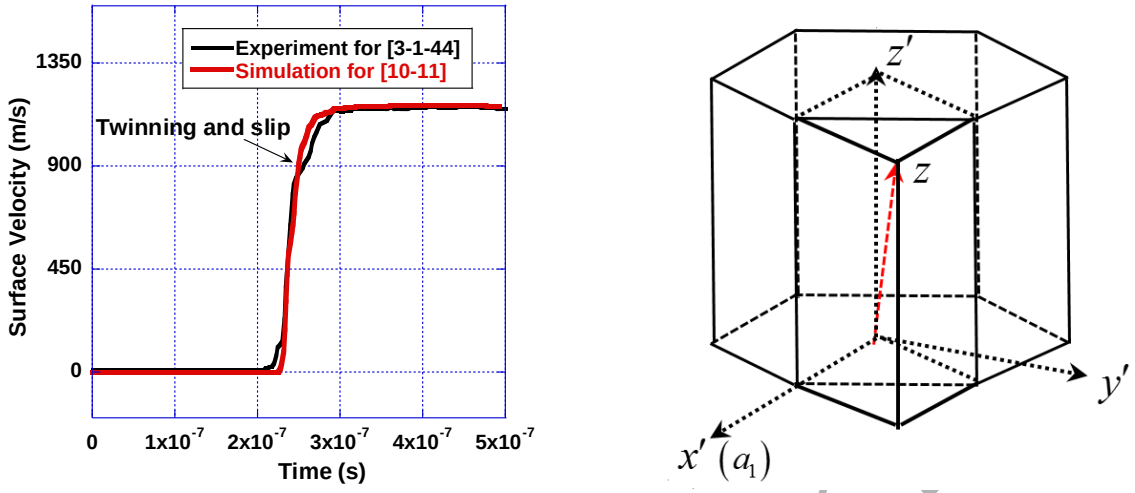

Fig. 10. (a) The free surface velocity from experiment for the $[3\bar{1}44]$ crystal and simulation for the $[10\bar{1}1]$ crystal. In the experiment, the crystal is loaded from the $[3\bar{1}44]$ direction, which is few degrees different from the direction $[10\bar{1}1]$ as in our simulation. In (b), the direction $[10\bar{1}1]$ of a single crystal is marked with a red arrow.

Fig. 11a shows the distribution of volume fractions for the parent material, total primary twins, total secondary twins, and total ω components for the $[10\bar{1}1]$ loaded crystal. The dominant material in the crystal is the parent material and after a stable compression at an axial position within the crystal of $z=5\times10^{-4}$ m it retains 0.712 volume fraction as shown in Fig. 11a. In the experiment, the parent material remains as 0.792 volume fraction after unloading as shown in Table 7. Primary twinning in the $[10\bar{1}1]$ crystal is not as prevalent as in the [0001] crystal, but secondary twinning is stronger in the $[10\bar{1}1]$ crystal as observed in both simulation and experiment. Primary twinning is less prevalent in the $[10\bar{1}1]$ crystal, due to a smaller Schmid factor and smaller resolved shear stress for primary twinning than that for the [0001] crystal orientation loading. However, primary twins in the $[10\bar{1}1]$ crystal have better orientations for secondary twinning than those in the [0001] crystal. The secondary twinning in the $[10\bar{1}1]$ crystal is significant as shown in Fig. 11. We did not find the ω phase in the experimental pole

figure, and the simulation result in Fig. 11 also shows that the volume fraction of the maximum ω component is 0.07 and the total ω phase is about 0.11 volume fraction.

As mentioned earlier, only the compressive portion of loading is considered. Fig.12 shows both experimental and simulated α phase pole figure results. These comparisons between the two results display some of the same final crystallographic state with combinations of parent material and primary and secondary twins, except that primary twin number 3 appears in Fig. 12b but does not appear in Fig. 12a. This primary twin completely transforms into secondary twins. In addition, we set a limit as 0.005, only above which phase transformation can occur. This threshold limit was necessary to enable proper representation of the evolution of both twinning and phase transformation simultaneously. More work will be necessary in the future to represent twinning on a more physical basis than what is commonly done. In addition, Fig. 12b shows that primary twin 3 is further twinned into four secondary twin variants, while primary twin 5 produces only two secondary twin variants. For this reason we did not find primary twin 3 in the experimental pole figure for shock loading. We did however find primary twin 3 in the results of SPHB loading in Feng *et al.*(2018a). There are 4 primary twin variants but only primary twin variants numbers 2 and 4 display phase transformation into ω component numbers 9 and 11. The orientations of these numbers for specific components can be found in the pole figure results.

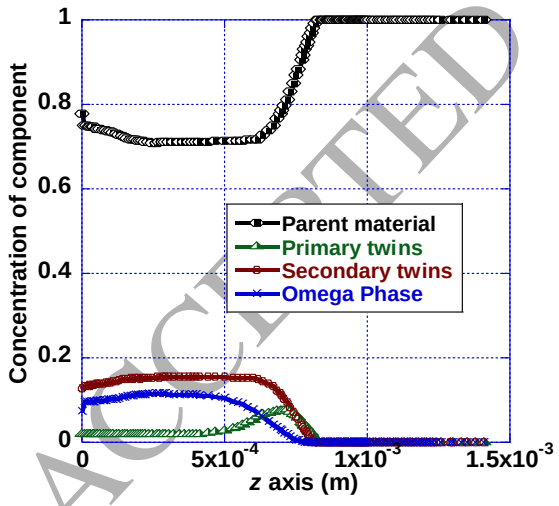

(a)

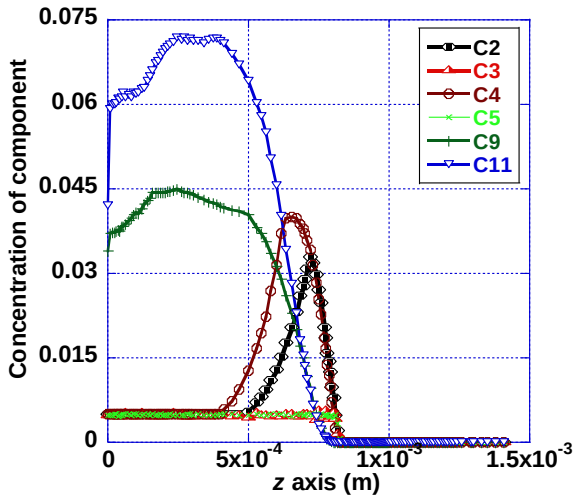

(b)

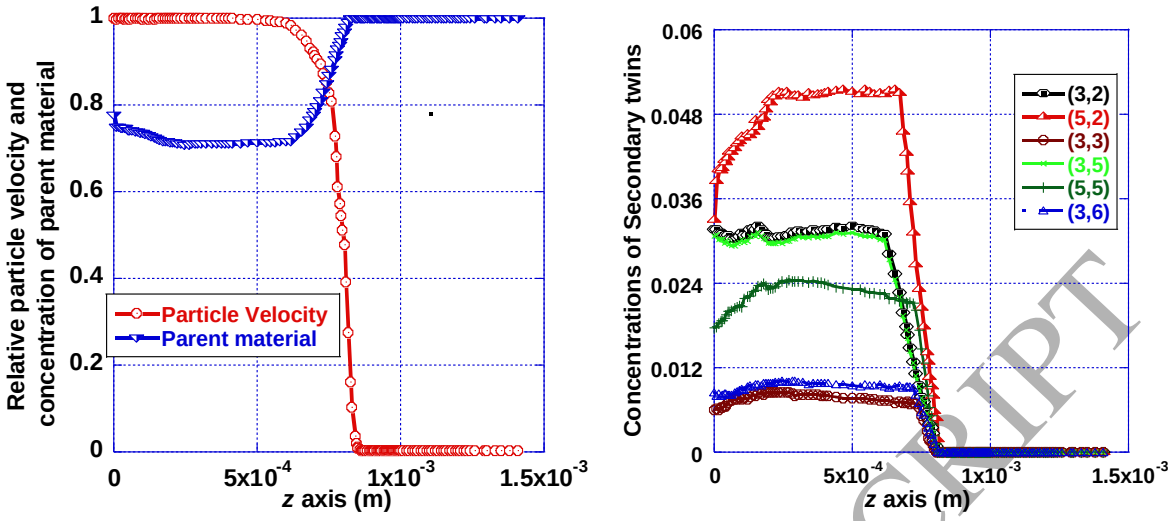

(c) (d)

Fig. 11. (a) Distributions in volume fractions of the parent material, total primary twins, total secondary twins, and total ω components. (b) the volume fractions of (c_0), each primary twin ($c_2 - c_5$) and the ω components (c_9 and c_{11}). (c) The relative particle velocity $\left(\frac{v}{600(\mathrm{m/s})}\right)$ and the volume fraction of total primary twins. (d) The volume fraction of each secondary twins, in which first number means twinning from which primary twin and the second number means twinning into which secondary twin. All figures are along the thickness direction (the *z*-axis) and the time instant is $t = 0.145\mu s$ for the $[10\bar{1}1]$ crystal orientation loading.

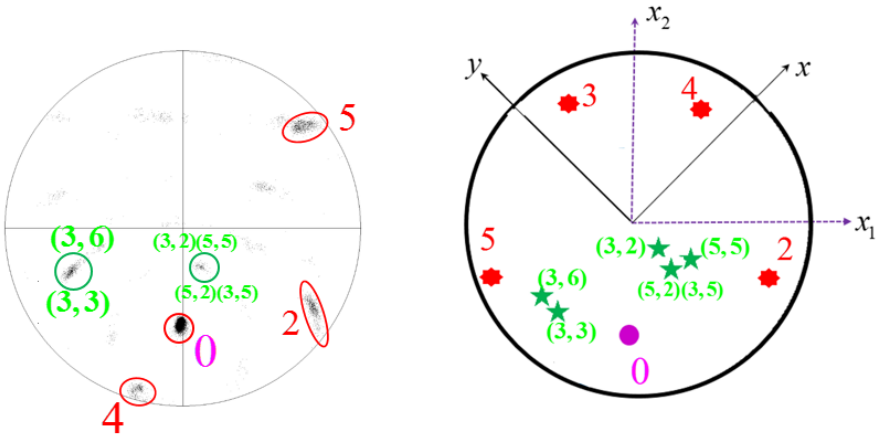

(a) (b)

Fig. 12. Pole figures for the α components from experiment (a) and simulation (b) for the $[10\bar{1}1]$ crystal orientation loading. Number 0 stands for the parent material, number 2-5 in red color are for primary twins, and the secondary twins are marked in green with two numbers in parentheses (the first number (3 and 5) indicates which primary twin variant they are from and the second number (2, 3, 5, 6) indicates four different tensile twinning variants). In experimental pole figure (a), the unmark region is negligible since the volume fraction is below than 4%.

Component	Volume fraction in experiment	Volume fraction in simulation
0	0.792	0.712
1	0.0	0.0
2	0.044	0.005
3	0.0	0.005
4	0.025	0.005
5	0.056	0.005
6	0.0	0.0
Secondary twins for marked places	0.046	0.156
Total above	0.963	0.888

Table 7. The volume fraction of the α phase components in experiment and simulation for the $[10\bar{1}1]$ crystal.

Fig. 13 plots the normal stress distribution along the thickness direction at $t = 0.145\,\mu s$. The axial normal stress σ_{zz} is much larger than the magnitudes of the stress components in the other two directions in Fig. 13, which causes a higher von Mises stress/shear stress than observed in the [0001] crystal. The σ_{xx} and σ_{yy} are very close, which is attributed to multiple slip systems and multiple twin and phase components, in addition to small anisotropy in the elastic properties in the HCP Ti. The peak pressure in the $[10\bar{1}1]$ orientation crystal is 14.2 GPa and is the same magnitude than the pressure in the [0001] orientation crystal. A lower volume fraction in primary twin variants and a faster secondary twinning process reduce the phase transformation driving force, in comparison with phase transformation in the [0001] oriented crystal. That is the reason why we did not find the ω phase to a significant degree in the $[10\bar{1}1]$ oriented crystal experiment and a very small amount of the ω phase during compression in simulation results.

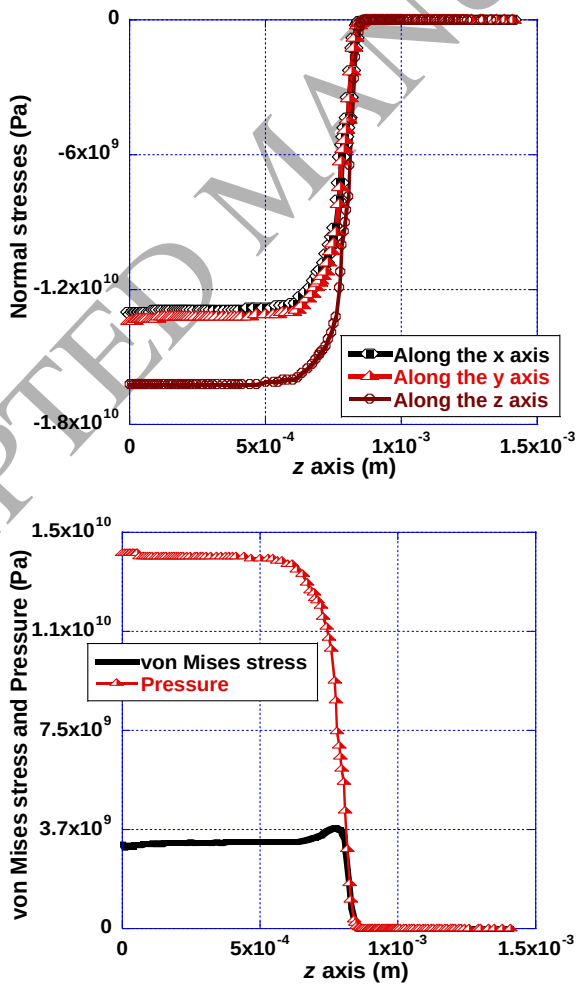

(a) (b)

Fig. 13. (a) Normal stresses $\left(\sigma_{xx}, \sigma_{yy}, \text{and } \sigma_{zz}\right)$, and (b) pressure and von Mises stress versus distance through the sample thickness for the $[10\bar{1}1]$ crystal orientation loading.

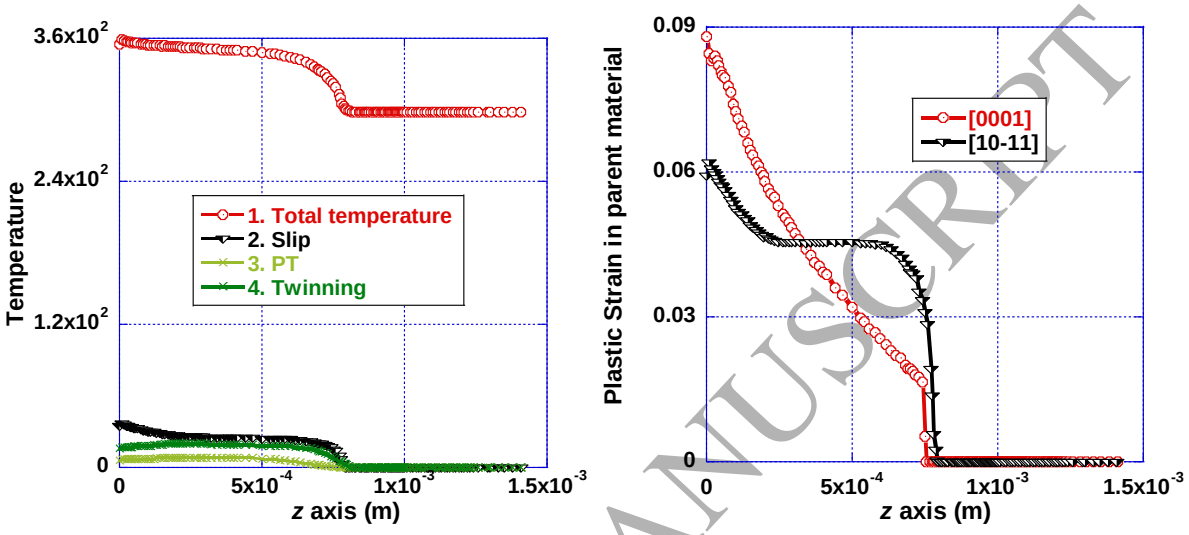

(a) (b)

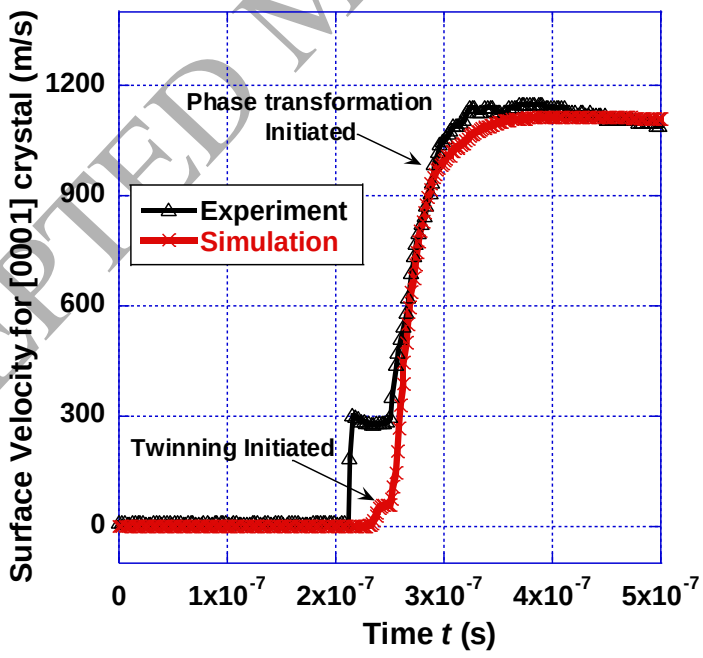

(c)

Fig. 14. Temperature distribution for the $[10\bar{1}1]$ crystal (a) and plastic strain (b) for parent material in the [0001] and $[10\bar{1}1]$ crystals. In (a), curve 1 is for the final temperature distribution, curves 2, 3, and 4 are the temperature increase due to slip, phase transformation, and twinning, respectively. In (c), the free surface velocity for the [0001] crystal in simulation is obtained by using the twinning threshold τ_{tw0} from the $[10\bar{1}1]$ crystal.

The evolution of temperature is shown in Fig. 14a. The initial reference temperature before compression is used as 298 K, and the final temperature after compression is around 360 K. This increase of temperature is mostly caused by dissipations during twinning and slip, which are larger than the contribution of phase transformation. In Fig. 14b we plot the plastic strain in the parent material for both the [0001] and $[10\bar{1}1]$ crystal orientations and the definition is given in Eq. (65). The threshold for twinning τ_{tw0} in Eq. (40) can be affected by the plastic slip. The dislocations densely pile up against the obstacles during plastic slip, which generates a strong concentrator of the stress tensor and can reduce τ_{tw0} (Levitas, 2004; Feng and Levitas, 2017a; Levitas and Javanbakht, 2015). First, as shown in Fig. 14 (b) plastic slip magnitude in the [0001] oriented crystal is significantly smaller than slip in the $[10\bar{1}1]$ oriented crystal in the region close to the elastic front and the primary twining only occurs in this region instead of the region close to impact plane as shown in Figs. 4 (a) and 11 (a). Second, Fig. 14a shows that the twinning and slip occurs at the same time for $[10\bar{1}1]$ crystal orientation, while the twining takes place earlier than plastic slip shown in Fig. 7. These two reasons cause a higher τ_{tw0} for the [0001] crystal, in comparison with the $[10\bar{1}1]$ crystal. If we use τ_{tw0} from the $[10\bar{1}1]$ crystal for the [0001] crystal in simulation, Fig. 14 (c) shows that both the plateau due to twinning and the slope decrease due to phase transformation can be reproduced the [0001] crystal in simulation, while the location of plateau happens in a lower velocity than experiment results.

11. Concluding remarks

In this paper, we present a thermodynamically consistent theory to model coupled nonlinear elasticity, plastic slip, deformation twinning, and phase transformation, in the kinematic framework of large deformation. The driving forces for plastic slip, twinning, and phase transformation are developed by utilizing the second law of thermodynamics. For nonlinear elasticity, the stiffness matrix is dependent on the volume fractions of all components, and the nonlinear equation of state is utilized for the volumetric part of the Cauchy stress. A dislocation density based plastic slip model for multi-component heterogeneous materials is developed and interactions of dislocations among all slip modes are taken into account. A mechanism for dislocation density evolution during twinning and phase transformation is proposed. High-purity single crystal Ti under high-strain rate loading in plate impact experiments are modeled and investigated, by using FEM. The system of constitutive equations is implemented into a user material subroutine (VUMAT) in ABAQUS/explicit.

The single crystals are loaded in the [0001] and $[10\bar{1}1]$ crystallographic directions in plate impact experiments are simulated. The evolutions of stress, strain, particle velocity, temperature, and volume fractions of components are obtained and discussed. The obtained results from simulation are used to assist in explaining and interpreting experimental observations. Reasonably good correspondence in the pole figures, volume fractions of components, free surface velocity, peak pressure, and phase transformation pressure between simulation and experiment is obtained. Differences between the simulation and experimental results were observed so more work in this area is required. Since the release process is not possible theoretically yet, some of this difference may be for this reason. However, challenges remain in understanding the coupled physical response of metallic materials to shock loading when multiple deformation mechanisms are active. The additional interfaces introduced to the material by twinning influences the mean-free path distances in the crystal and thereby effecting motion. Also, the mutual influence of dislocation structure and transformation events is known to take place, yet our ability to computationally represent is limited by the proper theories and the very high spatial resolution required. Even so, a great deal has been learned through this study and progress has been made in these directions within a continuum theory. It is found that the results are strongly dependent upon the impact loading directions of the single crystals.

For the [0001] crystal, there is a plateau in the free surface velocity curve during loading, which is caused by initiation of twinning, and the kink of the curve occurs due to the α to ω

phase transformation. The features of free surface are explained by the particle velocity and volume fraction of components through the sample thickness during compression, which are unavailable from experiment. Both simulation and experiment for the [0001] crystal orientation loading show primary twinning in six variants and six ω components, while the secondary twins are negligible. The intersection angles between the shock wave direction (i.e. the z-axis) and the twinning plane or twinning direction are the same for all six primary twin variants for the [0001] orientation crystal. As a result, the volume fractions for each primary twin and each ω component are reasonably similar in both simulation and experiment, although more work is necessary For the plate impact experiment, the strain is primarily one-dimensional but normal stress components are non-zero in all three axis directions. For the [0001] crystal, the normal stress $|\sigma_{zz}|$ along the shock direction is around 12% greater than the lateral stresses $|\sigma_{xx}|$ and $|\sigma_{yy}|$, and $|\sigma_{xx}|$ and $|\sigma_{yy}|$ are the same magnitude. In addition, the peak pressure is 14.2 GPa, consistent with experimental observation of 14.9 ± 0.2 GPa made in Morrow *et al*. (2017a). The phase transformation occurs at a pressure above 13.0 GPa, which is also consistent with experimental transition pressure estimated as 13.5 GPa. Such a pressure is much higher than the phase transformation pressure in Ti under static loading. Consequently, the phase transformation is strain rate dependent, and high strain-rate and short times impedes the kinetics of transformation. For the axial compressive deformation, the amount of twinning accumulated strain is slightly smaller than the elastic deformation, and both magnitudes are much larger than the axial deformation caused by both phase transformation and plastic slip.

Material responses for the [0001] and $[10\bar{1}1]$ crystals loaded by plate impact are very different. Primary twinning in the $[10\bar{1}1]$ crystal is not as prominent as in the [0001] crystal, but the secondary twinning is stronger in the $[10\bar{1}1]$ crystal as observed in both simulation and experiment. A lower volume fraction of primary twins and lower pressure in the $[10\bar{1}1]$ crystal reduce the phase transformation kinetics significantly, in comparison with phase transformation degree observed in the [0001] orientation loaded crystal. Consequently, we did not find the ω phase in the recovered $[10\bar{1}1]$ crystal after loading in experiment and only a very small amount of the ω phase during compression in simulation results. The increase in temperature in the

[0001] crystal is around 80 K due to twinning and phase transformation, while the change of temperature is smaller in the $[10\bar{1}1]$ crystal. Larger plastic deformation in the parent material can cause larger stress concentrators due to dislocation pileup during slip and thus a lower threshold for twinning τ_{tw0} for the $[10\bar{1}1]$ crystal, in comparison with the [0001] crystal.

It is significant that in this work, the experimental results could not be properly represented by a single set of material parameters. Specifically, the threshold for twinning τ_{tw0} in Eq. (40) is used differently for different loading orientations while all of other parameters are the same, and the reason for the variation of τ_{tw0} can be caused by the differences in the plastic slip as discussed in detail in Sec. 10. Although significant progress has been demonstrated, this is an indication that the theory described here is as yet still incomplete in properly representing the complex physics involved in this challenging problem. The results are however of significant benefit to understanding of material responses in the extreme conditions of high strain rate and high stresses, and the model developed in this paper also advances the mesoscale modeling and simulation in coupled plastic slip, deformation twinning, and phase transformations.

Acknowledgements

The authors gratefully acknowledge support for this work from Los Alamos National Laboratory Campaign 2 Dynamic Materials program, and the Advanced Simulation and Computing program. Fruitful discussions and numerical assistance from Dr. H. Mourad are also gratefully acknowledged.

References

Abdolvand, H., Daymond, M.R., 2013. Multi-scale modeling and experimental study of twin inception and propagation in hexagonal close-packed materials using a crystal plasticity finite element approach part I: average behavior. J. Mech. Phys. Solids 61, 783-802.

Abdolvand, H., Daymond, M.R., Mareau, C., 2011. Incorporation of twinning into a crystal plasticity finite element model: Evolution of lattice strains and texture in Zircaloy-2. Int. J. Plast. 27, 1721-1738.

Abdolvand, H., Majkut, M., Oddershede, J., Schmidt, S., Lienert, U., Diak, B.J., Withers, P.J., Daymond, M.R., 2015. On the deformation twinning of Mg AZ31B: a three-dimensional synchrotron X-ray diffraction experiment and crystal plasticity finite element model. Int. J. Plast. 70, 77-97.

Addessio, F.L., Luscher, D.J., Cawkwell, M.J., Ramos, K.J., 2017. A single-crystal model for the high-strain rate deformation of cyclotrimethylene trinitramine including phase transformations and plastic slip. J. Appl. Phys. 121, 185902.

Akahama, Y., Kawamura, H., Le, Bihan T., 2001. New δ (Distorted-bcc) titanium to 220 GPa. Phys. Rev. Lett. 87 275503.

Akahama, Y., Kawamura, H., Le Bihan, T., 2002. A new distorted body-centred cubic phase of titanium (δ-Ti) at pressures up to 220 GPa. J. Phys. Condens. Matter 14, 10583-10588.

Ardeljan, M., McCabe, R.J., Beyerlein, I.J., Knezevic, M., 2015. Explicit incorporation of deformation twins into crystal plasticity finite element models. Comput. Methods Appl. Mech. Eng. 295, 396-413.

Barton, N. Benson, D. J., Becker, R., 2005. Crystal level continuum modeling of phase transformations: the α ↔ ε transformation in iron. Modelling Simul. Mater. Sci. Eng. 13, 707-731.

Becker, R., 2004. Effects of crystal plasticity on materials loaded at high pressures and strain rates, Int. J. Plast. 20, 1983-2006.

Beyerlein, I.J., Tome, C.N., 2008. A dislocation-based constitutive law for pure Zr including temperature effects. Int J Plast. 24, 867-895.

Beyerlein, I.J., Capolungo, L., Marshall, P.E., McCabe, R.J., Tome, C.N., 2010. Statistical analyses of deformation twinning in magnesium. Philos. Mag . 90, 4073-4074.

Beyerlein, I.J., Tome, C.N., 2010. A probabilistic twin nucleation model for HCP polycrystalline metals. Proc. R. Soc. A 466, 2517-2544.

Beyerlein, I.J., McCabe, R.J., Tome, C.N., 2011. Stochastic processes of {1012} deformation twinning in hexagonal close-packed polycrystalline zirconium and magnesium. Int. J. Multiscale Com. 9, 459-480.

Bezruchko, G.S., Razorenov, S.V., Kanel, G.I., Fortov, V.E., 2006. Influence of temperature upon the α-ω transition in titanium. AIP Conf. Proc. 845, 192–195.

Bronkhorst, C.A., Kalidindi, S.R., Anand, L., 1992. Polycrystal plasticity and the evolution of crystallographic texture in FCC metals. Philosophical Transactions: Phys. Sci. Eng. 341, 443-477.

Cerreta, E.K., Gray Iii, G.T., Hixson, R.S., Rigg, P.A., Brown, D.W., 2005. The influence of interstitial oxygen and peak pressure on the shock loading behavior of zirconium. Acta Mater. 53, 1751-1758.

Cerreta E.K., Gray G.T. III, Lawson A.C., Morris C.E., Hixson R.S., Rigg P.A., 2006a. The influence of interstitial oxygen on the alpha to omega phase transition in titanium and zirconium. AIP Conf. Proc. 845, 1149–1152.

Cerreta, E.K., Gray III, G.T., Lawson, A.C., Mason, T.A., Morris, C.E., 2006b. The influence of oxygen content on the α to ω phase transformation and shock hardening of titanium. J. Appl. Phys. 100 013530.

Cheng, J., Ghosh, S., 2015. A crystal plasticity FE model for deformation with twin nucleation in magnesium alloys. Int. J. Plast. 67, 148-170.

Cheng, J., Ghosh, S., 2017. Crystal plasticity finite element modeling of discrete twin evolution in polycrystalline magnesium. J. Mech. Phys. Solids 99, 512-538.

Cheng, J., Shen, J., Mishra, R. K., Ghosh, S., 2018. Discrete twin evolution in Mg alloys using a novel crystal plasticity finite element model. Acta Mater. 149, 142-153.

Clayton, J.D., 2010. Nonlinear mechanics of crystals. Springer, New York.

Clouet, E., Caillard, D., Chaari, N., Onimus, F., Rodney, D., 2015. Dislocation locking versus easy glide in titanium and zirconium. Nat. Mater. 14, 931-937.

Cuitino, A., Ortiz, M. 1993. Constitutive modeling of 112 intermetallic crystals. Mat. Sci. Eng. a-Struct. 170, 111-123.

Feng, B., Bronkhorst, Addessio, F.L., Morrow, B.M., Cerreta, E.K., Lookman, T. Lebensohn, R.A., and Low T., 2018a. Coupled elasticity, plastic slip, and twinning in single crystal titanium loaded by split-Hopkinson pressure bar. J. Mech. Phys. Solids 119, 274-297.

Feng, B., Levitas, V.I., 2017a. Coupled Elastoplasticity and Plastic Strain-Induced Phase Transformation under High Pressure and Large Strains: Formulation and Application to BN Sample Compressed in a Diamond Anvil Cell. Int. J. Plast. 96, 156-181.

Feng, B., Levitas, V.I., 2017b. Large elastoplastic deformation of a sample under compression and torsion in a rotational diamond anvil cell under megabar pressures. Int. J. Plast. 92, 79-95.

Feng, B., Levitas, V.I., 2017c. Plastic flows and strain-induced alpha to omega phase transformation in zirconium during compression in a diamond anvil cell: Finite element simulations. Mat. Sci. Eng. a-Struct. 680, 130-140.

Feng, B., Levitas, V.I., Hemley, R.J., 2016. Large elastoplasticity under static megabar pressures: Formulation and application to compression of samples in diamond anvil cells. Int. J. Plast. 84, 33-57.

Feng, B., Levitas, V. I., and Kamrani, M. 2018b. Coupled strain-induced alpha to omega phase transformation and plastic flow in zirconium under high pressure torsion in a rotational diamond anvil cell. Mat. Sci. Eng. A-Struct. 731, 623-633.

Fisher, E.S., Renken, C.J., 1964. Single-Crystal Elastic Moduli and HCP to BCC Transformation in Ti, Zr, and Hf. Phys. Rev. a-Gen. Phys. 135, A482-A494.

Greeff, C.W., Trinkle, D.R., Albers, R.C., 2001. Shock-induced alpha-omega transition in titanium. J. Appl. Phys. 90, 2221-2226.

Greeff, C.W., Rigg, P.A,, Knudson, M.D., Gray, G.T. III, 2004. Modeling dynamic phase transitions in Ti and Zr. AIP Conf. Proc. 706, 209–212.

Ghosh, S., Cheng, J., 2018. Adaptive multi-time-domain subcycling for crystal plasticity FE modeling of discrete twin evolution. Comput. Mech. 61, 33-54.

Ghosh, P.S., Arya, A., Tewari, R., Dey, G.K., 2014. Alpha to omega martensitic phase transformation pathways in pure Zr. J. Alloy. Compd. 586, 693-698.

Gong, J.C., Britton, T.B., Cuddihy, M.A., Dunne, F.P.E., Wilkinson, A.J., 2015. < a > Prismatic, < a > basal, and < c + a > slip strengths of commercially pure Zr by micro-cantilever tests. Acta Mater. 96, 249-257.

Hama, T., Kobuki, A., Takuda, H., 2017. Crystal-plasticity finite-element analysis of anisotropic deformation behavior in a commercially pure titanium Grade 1 sheet. Int. J. Plast. 91, 77-108.

Hansen, B.L., Beyerlein, I.J., Bronkhorst, C.A., Cerreta, E.K., Dennis-Koller, D., 2013. A dislocation-based multi-rate single crystal plasticity model. Int. J. Plast. 44, 129-146.

Hao, Y.-J., Zhu, J., Zhang, L., Qu, J.-Y., Ren, H.-S., 2010. First-principles study of high pressure structure phase transition and elastic properties of titanium. Solid State Sci. 12, 1473–1479.

Irgens, F., 2008. Continuum mechanics. Springer, Berlin.

Javanbakht, M., Levitas, V.I., 2015. Interaction between phase transformations and dislocations at the nanoscale. Part 2: Phase field simulation examples. J. Mech. Phys. Solids 82, 164-185.

Jayaraman, A., Klement, J.W., Kennedy, G.C., 1963. Solid-solid transitions in titanium and zirconium at high pressures. Phys. Rev. 131, 644.

Jones, D.R., Morrow, B.M., Trujillo, C.P., Gray, G.T., Cerreta, E.K., 2017. The α–ω phase transition in shock-loaded titanium. J. Appl. Phys. 122, 045902.

Kannan, V., Hazeli, K., Ramesh, K.T., 2018. The mechanics of dynamic twinning in single crystal magnesium. J. Mech. Phys. Solids, 120, 154-178.

Kalidindi, S.R., 1998. Incorporation of deformation twinning in crystal plasticity models. J. Mech. Phys. Solids 46, 267-290.

Lieou, C. K. C., Bronkhorst, C. A., 2018. Dynamic recrystallization in adiabatic shear banding: effective-temperature model and comparison to experiments in ultra-fine grained titanium. Int. J. Plasticity, in press.

Lieou, C. K. C., Mourad, H. M., Bronkhorst, C. A., 2018. Strain localization and dynamic recrystallization in polycrystalline metals: thermodynamic theory and simulation framework. Int. J. Plasticity, submitted.

Levitas, V. I., 2004. High pressure mechanochemistry: conceptual multiscale theory and interpretation of experiments. Phys. Rev. B 70, 184118.

Levitas, V.I., Javanbakht, M., 2015. Interaction between phase transformations and dislocations at the nanoscale. Part 1. General phase field approach. J. Mech. Phys. Solids 82, 287-319.

Levitas, V. I., Ma, Y. Z., Hashemi, J., Holtz, M., and Guven, N., 2006. Strain-induced disorder, phase transformations, and transformation-induced plasticity in hexagonal boron nitride under compression and shear in a rotational diamond anvil cell: In situ x-ray diffraction study and modeling. J. Chem. Phys. 125, 044507.

Luscher, D.J., Addessio, F.L., Cawkwell, M.J., Ramos, K.J., 2017. A dislocation density-based continuum model of the anisotropic shock response of single crystal α-cyclotrimethylene trinitramine. J. Mech. Phys. Solids 98, 63-86.

Luscher, D.J., Buechler, M.A., Walters, D.J., Bolme, C.A., Ramos, K.J., 2018. On computing the evolution of temperature for materials under dynamic loading. Int. J. Plast. (In press)

Montgomery, J.S., Wells, M.G.H., Roopchand, B., 1997. Low-cost titanium armors for combat vehicles. JOM-US 49, 45–47.

Morrow, B.M., Lebensohn, R.A., Trujillo, C.P., Martinez, D.T., Addessio, F.L., Bronkhorst, C.A., Lookman, T., Cerreta, E.K., 2016. Characterization and modeling of mechanical behavior of single crystal titanium deformed by split-Hopkinson pressure bar. Int J Plast. 82, 225-240.

Morrow, B.M., Rigg, P.A., Jones, D.R., Addessio, F.L., Escobedo, J.P., Trujillo, C.P., Saavedra, R.A., Martinez, D.T., Cerreta, E.K., 2017a. Shock and Microstructural Characterization of the alpha to omega Phase Transition in Titanium Crystals. J. Dynamic Behavior Mater. 3, 526-533.

Morrow, B.M., Escobedo, J.P., Field, R.D., Dickerson, R.M., Dickerson, P.O., Trujillo, C.P., Cerreta, E.K., 2017b. Examination of the alpha-omega Two-Phase Shock-Induced Microstructure in Zirconium and Titanium. AIP Conf. Proc. 1793, 100033.

Nervo, L., King, A., Fitzner, A., Ludwig, W., Preuss, M., 2016. A study of deformation twinning in a titanium alloy by X-ray diffraction contrast tomography. Acta Mater. 105, 417-428.

Niezgoda, S.R., Beyerlein, I.J., Kanjarla, A.K., Tome, C.N., 2013. Introducing Grain Boundary Influenced Stochastic Effects into Constitutive Models. JOM-US 65, 419-430.

Niezgoda, S.R., Kanjarla, A.K., Beyerlein, I.J., Tome, C.N., 2014. Stochastic modeling of twin nucleation in polycrystals: An application in hexagonal close-packed metals. Int. J. Plast. 56, 119-138.

Razorenov, S.V., Utkin, A.V., Kanel, G.I., Fortov, V.E., Yarunichev, A.S., Baumung, K., Karow, H.U., 1995. Response of high-purity titanium to high-pressure impulsive loading. High Pres. Res. 13, 367-376.

Sachdev, A.K., Kulkarni, K., Fang, Z.Z., Yang, R., Girshov, V., 2012. Titanium for automotive applications: challenges and opportunities in materials and processing. JOM-US 64, 553-565.

Salem, A.A., Kalidindi, S.R., Doherty, R.D., 2003. Strain hardening of titanium: role of deformation twinning. Acta Mater. 51, 4225-4237.

Salem, A.A., Kalidindi, S.R., Semiatin, S.L., 2005. Strain hardening due to deformation twinning in alpha-titanium: Constitutive relations and crystal-plasticity modeling. Acta Mater. 53, 3495-3502.

Sargent, G., Conrad, H., 1971. Formation of the omega phase in titanium by hydrostatic pressure soaking. Mater. Sci. Eng. 7, 220-223.

Saxena, A.K., Kaushik, T.C., Gupta, S.C., 2015. Shock loading characteristics of Zr and Ti metals using dual beam velocimeter. J. Appl. Phys. 118 075904.

Shoesmith, D.W., Noel, J.J., Hardie, D., Ikeda, B.M., 2000. Hydrogen absorption and the lifetime performance of titanium nuclear waste containers. Corros. Rev. 18, 331-360.

Sikka, S. K., Vohra, Y.K., Chidambaram, R., 1982. Omega phase in materials. Prog. Mater. Sci. 27, 245-310.

Singh, A.K., Mohan, M., Divakar, C., 1982. The kinetics of pressure-induced $\alpha \rightarrow \omega$ transformation in Ti. J. Appl. Phys. 53, 1221-1223.

Tome, C.N., Maudlin, P.J., Lebensohn, R.A., Kaschner, G.C., 2001. Mechanical response of zirconium—I. Derivation of a polycrystal constitutive law and finite element analysis. Acta Mater. 49, 3085-3096.

Trinkle, D.R., Hennig, R.G., Srinivasan, S.G., Hatch, D.M., Jones, M.D., Stokes, H.T., Albers, R.C., Wilkins, J.W., 2003. New mechanism for the α to ω martensitic transformation in pure titanium. Phys. Rev. Lett. 91, 025701.

Xia, H., Parthasarathy, G., Luo, H., Vohra, Y.K., Ruoff, A., 1990. Crystal structures of group IVa metals at ultrahigh pressures. Phys. Rev. B 42, 6736-6738.

Vohra, Y.K., 1978. Kinetics of phase transformations in Ti, Zr and Hf under static and dynamic pressures. J. Nucl. Mater. 75, 288-293.

Vohra, Y.K., Spencer, P.T., 2001. Novel γ-phase of titanium metal at megabar pressures. Phys. Rev. Lett. 86, 3068-3071.

Wang, H., Wu, P.D., Wang, J., Tome, C.N., 2013. A crystal plasticity model for hexagonal close packed (HCP) crystals including twinning and de-twinning mechanisms. Int. J. Plast. 49, 36-52.

Winey, J.M., Gupta, Y.M., 2006. Nonlinear anisotropic description for the thermomechanical response of shocked single crystals: Inelastic deformation . J. Appl. Phys. 99, 023510.

Winey, J.M., Gupta, Y.M., 2010. Anisotropic material model and wave propagation simulations for shocked pentaerythritol tetranitrate single crystals. J. Appl. Phys. 107, 103505.

Yeddu, H.K., Zong, H., Lookman, T., 2016. Alpha-omega and omega-alpha phase transformations in zirconium under hydrostatic pressure: a 3D mesoscale study. Acta Mater. 102, 97-107.

Yoo, M.H., Agnew, S.R., Morris, J.R., Ho, K.M., 2001. Non-basal slip systems in HCP metals and alloys: source mechanisms. Mat. Sci. Eng. a-Struct. 319, 87-92.

Zhang, L., Li, Y. H., Cai, L.C. 2018. A formulism of two-phase equilibrium and phase diagram for elastic-plastic deformed system under non-hydrostatic stress conditions: Formulations and verification. Int. J. Plast. 104, 147-172.

Zong, H.X., Lookman, T., Ding, X. D., Luo, S.N., Sun, J., 2014. Anisotropic shock response of titanium: Reorientation and transformation mechanisms. Acta Mater. 65, 10-18.